

# Long-Integration Magnetar Burst Observatory (LIMBO): Instrument Summary and Early FRB Rate Constraints

Darby McCauley <sup>1,2\*</sup> Aaron Parsons <sup>2,3</sup> Wei Liu <sup>3</sup> Wenbin Lu <sup>2,4</sup> Dirk Wright,<sup>3</sup> and Dan Werthimer<sup>3,5</sup>

<sup>1</sup>Department of Astronomy, University of Illinois Urbana-Champaign, Urbana, IL 61801, USA

<sup>2</sup>Department of Astronomy, University of California, Berkeley, Berkeley, CA 94720, USA

<sup>3</sup>Radio Astronomy Laboratory, University of California, Berkeley, Berkeley, CA 94720, USA

<sup>4</sup>Theoretical Astrophysics Center, University of California, Berkeley, Berkeley, CA 94720, USA

<sup>5</sup>Space Sciences Laboratory, University of California, Berkeley, Berkeley, CA 94720, USA

Accepted XXX. Received YYY; in original form ZZZ

## ABSTRACT

The Long-Integration Magnetar Burst Observatory (LIMBO) is a real-time radio transient detection pipeline designed to search for dispersed fast radio bursts (FRBs) from Galactic magnetars. Deployed at the University of California, Berkeley’s Leuschner Radio Observatory, LIMBO employs a 4.3-m dish with a dual-polarization feed to continuously monitor a 250 MHz band centred at 1475 MHz. A real-time processing pipeline performs a search for dispersed transients on the summed polarizations, with detections triggering dumps of buffered voltage data to disk. Based on calibrated sensitivity measurements, synthetic signal-injection and recovery tests, and successful detection of pulses from the Crab Pulsar, we determine that LIMBO is sensitive to radio transients with fluences  $\geq 43 \text{ Jy} \cdot \text{ms}$ . Between May and August 2023, LIMBO conducted 833 hours of follow-up observations of the Galactic magnetar SGR 1935+2154, yielding 12 candidate FRB detections. If these events are true, we measure FRB-like event rates from SGR 1935+2154 of  $R(\geq 65 \text{ Jy} \cdot \text{ms}) = 112.3^{+81.3}_{-54.5} \text{ yr}^{-1}$  and  $R(\geq 130 \text{ Jy} \cdot \text{ms}) = 17.7^{+40.8}_{-15.1} \text{ yr}^{-1}$ . Combining these results with previously reported FRBs from SGR 1935+2154, we infer a cumulative rate–fluence power-law slope of  $\alpha = -0.60^{+0.24}_{-0.28}$  in the fluence range between 10 and  $10^6 \text{ Jy} \cdot \text{ms}$ . These observations demonstrate the capability of continuous, real-time monitoring of Galactic magnetars and establish LIMBO as an effective instrument for detecting Galactic FRBs.

**Key words:** Fast Radio Bursts – Radio transient sources – Magnetars – Instrumentation – Telescopes

## 1 INTRODUCTION

Fast radio bursts (FRBs) are bright, millisecond-duration radio transient events. The first FRB was identified in 2007 through retrospective analysis of archival data from the Parkes radio telescope (Lorimer et al. 2007). Since then, hundreds to thousands of FRBs have been detected, with dispersion measures (DMs) often significantly exceeding the Galactic contribution, implying extragalactic and cosmological origins (Thornton et al. 2013; Petroff et al. 2016; Cordes & Chatterjee 2019). While the majority of FRBs appear to be one-off events, a subset has been observed to repeat (Spitler et al. 2016; Chime/Frb Collaboration et al. 2023).

These discoveries have been driven primarily by wide-field, high-cadence survey instruments, with major contributions from Parkes (Thornton et al. 2013; Champion et al. 2016; Bhandari et al. 2018), CHIME (CHIME/FRB Collaboration et al. 2018, 2021, 2026), ASKAP (Bannister et al. 2017; Shannon et al. 2018), UTMOST (Bailes et al. 2017; Caleb et al. 2017), FAST (Li et al. 2018; Niu et al. 2021), STARE-2 (Bochenek et al. 2020a), ATA (Welch et al. 2009; Sheikh et al. 2024), and Apertif (Maan & van Leeuwen 2017; Oostrum et al. 2020), among others.

Although FRBs were first identified more than a decade ago, their physical origin and emission mechanism remain poorly understood,

making them a compelling focus of astrophysical research. Despite the large number of detections to date, nearly all have been observed at cosmological distances, making it difficult to definitively identify their progenitors, local environments, or emission processes. However, the detection of a bright radio burst from the Galactic magnetar SGR 1935+2154 temporally coincident with an X-ray flare provides strong evidence that at least some FRBs are produced by magnetars (Bochenek et al. 2020b; CHIME/FRB Collaboration et al. 2020; Mereghetti et al. 2020; Ridnaia et al. 2021; Li et al. 2021). This discovery has opened a promising pathway for constraining FRB emission mechanisms through detailed multi-wavelength observations of nearby magnetars. Follow-up observations of SGR 1935+2154 have resulted in successful repeat FRB detections (Zhang et al. 2020; Kirsten et al. 2021; Zhu et al. 2023; Dong & Chime/Frb Collaboration 2022; Maan et al. 2022; Huang et al. 2022; Pearlman & Chime/Frb Collaboration 2022).

Despite growing evidence linking at least a subset of FRBs to magnetars, the conditions under which these magnetars produce these radio bursts remain poorly constrained. Proposed emission mechanisms are broadly divided between magnetospheric processes and relativistic shock models (Kumar et al. 2017; Lu et al. 2020; Metzger et al. 2019; Beloborodov 2020; Margalit et al. 2020). Extragalactic detections, however, are limited by energy thresholds ( $E \sim 10^{36-41}$  ergs), sparse temporal coverage, and the inability to resolve progenitor sources via e.g., X-ray counterparts and supernova remnants. This

\* E-mail: darbyn2@illinois.edu

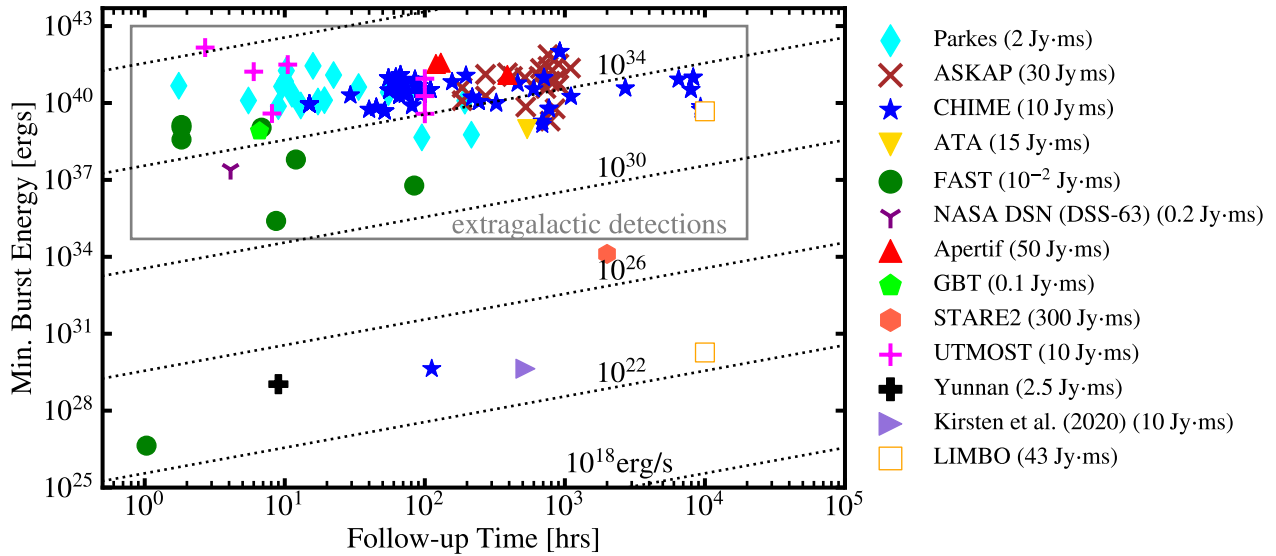


**Figure 1.** Minimum FRB burst energy versus follow-up observation time for a range of FRB projects. For extragalactic sources, each symbol represents a different FRB source as observed by a given instrument; the symbols outside the "extragalactic detections" region represent FRBs originating from the Galactic magnetar SGR 1935+2154 but detected by different instruments. For comparison, we show LIMBO's minimum detectable burst energy in both the Galactic and extragalactic (assumed redshift of  $z = 0.1$ ) regimes.

makes it difficult to characterize how the FRBs emission is correlated to their progenitor activities, although population modelling provides strong constraints on their cosmological rates and source objects (Shin et al. 2023; Kirsten et al. 2024).

By contrast, long-term radio-frequency monitoring of Galactic magnetars for FRB activity offers a powerful approach to addressing these challenges. Targeting Galactic sources significantly reduces energy thresholds by orders of magnitude, making low-energy bursts observable. Furthermore, sustained, extended, and source-resolved follow-up observations of FRB producing Galactic sources are critical for discriminating different FRB emission mechanisms. In this way, dedicated single-dish facilities provide access to burst properties and temporal behaviours that are largely inaccessible to wide-field extragalactic surveys.

We present the Long-Integration Magnetar Burst Observatory (LIMBO), a real-time detection pipeline employed on the 4.3-m radio telescope at the University of California, Berkeley's Leuschner Observatory, optimized to perform long observational campaigns of Galactic magnetars and study the FRBs they produce. As illustrated in Figure 1, a key strength of LIMBO is its capacity to accumulate  $\sim 10^4$  hours of follow-up observations, coupled with the sensitivity to detect faint Galactic FRBs, enabling exploration of a region of parameter space that has previously remained inaccessible.

We organize the paper as follows. In Section 2, we describe the LIMBO instrument, including both its analogue and digital sub-systems. Section 3 details calibration procedures, radio-frequency interference (RFI) excision techniques, and the real-time radio transient detection pipeline. In Section 4, we demonstrate signal-injection/recovery tests and detection of giant pulses from the Crab Pulsar. Observational targets and candidate FRB detections from SGR 1935+2154 using LIMBO are presented alongside inferred rate constraints in Section 5. Finally, we summarize results in Section 6 and discuss the role of long-term, single-dish follow-up observations in advancing our understanding of FRBs.

## 2 THE OBSERVING SYSTEM

LIMBO operates with a 4.3-m radio dish at the University of California, Berkeley's Leuschner Student Observatory, located at  $(-122^\circ 9' 12.31'', +37.8732^\circ)$ , approximately 30 miles from the UC Berkeley campus in the hills of Lafayette, CA. The dish, mounted on an alt-az drive, covers a declination range of  $53^\circ$  to  $123^\circ$ , with an effective beam solid angle of  $\sim 0.003$  sr and a bandwidth of 250 MHz (see Table 1 for additional details and Figure 2).

### 2.1 The Analogue System

The Leuschner Radio Telescope is equipped with a dual-polarization, wide-band, quadruple-ridged, flared horn feed (Shi et al. 2017), un-cooled low-noise amplifiers (LNAs), and radio-frequency-over-fibre (RFoF) modules that transmit signals over a 100-m link to an indoor processing rack for further amplification, down-conversion, filtering, and digital sampling. A block diagram of the LIMBO system is shown in Figure 3.

LIMBO processes two linear polarization signal streams through parallel analogue signal chains with matched characteristics. Each signal first passes through an LNA covering 0.8–2.5 GHz, after which it is bandpass filtered to 1.2–2.5 GHz. Additional amplification is provided by Mini-Circuits ZJL-7G+ and ZVA-183+ modules, with anti-reflection attenuation, before transmission via fibre-optic link using a Photonic Systems Inc. transmitter (PSI-1600-10UT) and receiver (PSI-1600-10UR).

Within the observatory's control room, signals are filtered by a  $1515 \pm 115$  MHz bandpass filter, then heterodyne mixed to base-band and further filtered to yield a total observable RF range of 1400–1524 MHz. An Agilent N9310A RF signal generator, set to 1.35 GHz, serves as the local oscillator (LO).



**Figure 2.** The 4.3-m radio telescope located at the UC Berkeley Leuschner Radio Observatory, equipped with the LIMBO FRB detection pipeline.

## 2.2 The Digital System

Analogue signals are digitized and packetized using a Smart Network ADC Processor (SNAP<sup>1</sup>) board developed by the Collaboration for Astronomy Signal Processing and Electronics Research (CASPER) (DeBoer et al. 2017; Hickish et al. 2016). Each of two 8-bit analogue-to-digital converters (ADCs) is clocked at 500 MHz, providing a Nyquist bandwidth of 250 MHz per polarization stream. The digitized signals are routed to the board’s Kintex-7 field-programmable gate array (FPGA), which performs real-time digital signal processing.

LIMBO employs a modified version of the DSA-10 SNAP design (Kocz et al. 2019), adapted to accommodate a different number of ADC inputs. FPGA firmware is designed using CASPER libraries. A polyphase filter bank (PFB), consisting of a 4-tap, 4096-point finite impulse response (FIR) filter followed by a real-valued fast Fourier transform (FFT), converts the time-domain data into the frequency domain (Parsons 2009). This produces 2048 frequency channels with a spectral resolution of 122 kHz. The PFB output is then divided into two parallel spectral streams: a power stream and a voltage stream, each retaining 18-bit real and imaginary components. A block diagram of the LIMBO digital system is shown in Figure 4.

Power spectra are integrated over 128 consecutive time windows, yielding a time resolution of 1 ms. The data are then rescaled to signed 16-bit integers before being transmitted to the server over a 10-Gb Ethernet connection. Similarly, voltage spectra from both

polarizations are rescaled and quantized to signed 8-bit (4b real, 4b imaginary) complex integer format before being streamed to the server via a second 10-Gb Ethernet connection.

Both Ethernet streams employ the HASHPIPE data transfer protocol<sup>2</sup>. The voltage spectra have a native time resolution of 8.192  $\mu$ s and an aggregate data rate of  $\sim$ 4 Gbps. These data are written to a 16-GB memory-mapped ring buffer on a CPU server, where they are retained for up to 16 s. During this interval, real-time analysis and statistical thresholding are applied to the integrated power spectra to search for dispersed transient signals, as described below.

## 3 LIMBO ANALYSIS

The LIMBO real-time analysis system operates on integrated power spectra in 4-s blocks to decide whether voltage spectra stored in the ring buffer should be overwritten or offloaded to long-term storage for follow-up analysis. The objective is to identify potential dispersed pulses with a negligible false-negative rate, while maintaining a false-positive rate low enough to minimize unnecessary data transfers that could delay processing and inflate storage and post-processing costs.

The real-time system incorporates gain and phase calibration, RFI excision, de-trending, statistical characterization, and an initial detection pipeline. Each of these components is described in detail below.

### 3.1 Calibration

To obtain accurate measurements of flux density and polarization, we perform both a gain calibration and a polarization phase alignment. At LIMBO’s observing frequencies, the measured sky signal is dominated by diffuse Galactic synchrotron emission. As a result, observations of a well-characterized calibrator source provide a robust means of isolating the instrumental response and characterizing the frequency-dependent system temperature. Paired observations of Cygnus A (Baars et al. 1977) and a nearby cold-sky position (20h 10m 30.44s, +40° 43′ 34.31″) are used to derive a frequency-dependent gain factor, enabling the conversion of measured power into absolute flux density. To account for residual flux from Cygnus A remaining within the beam, we model the beam as Gaussian and explicitly incorporate the resulting contamination into the derived gain factor.

To estimate the receiver temperature  $T_{rx}$ , we account for the sky contribution using the Global Sky Model 2016 (Price 2016). We convolve Leuschner’s beam with the all-sky continuum map to determine the expected sky temperature at 1420 MHz. Centring the beam on the coordinates of SGR 1935+2154, we measure an antenna temperature of 5.68 K for the local sky environment. Subtracting this contribution from the total system temperature  $T_{sys}$ , we obtain a receiver temperature of 47.34 K at 1420 MHz. This and other properties of the Leuschner radio telescope are summarized in Table 1.

For phase calibration, we use injected electromagnetic pulses to measure the relative phase difference between the two voltage streams. By correlating the injected signals, we determine the delay offset, which is corrected by applying a complex per-frequency phase adjustment to one of the streams. This procedure yields the final phase calibration.

<sup>1</sup> <https://casper.astro.berkeley.edu/wiki/SNAP>

<sup>2</sup> <https://github.com/david-macmahon/hashpipe.git>

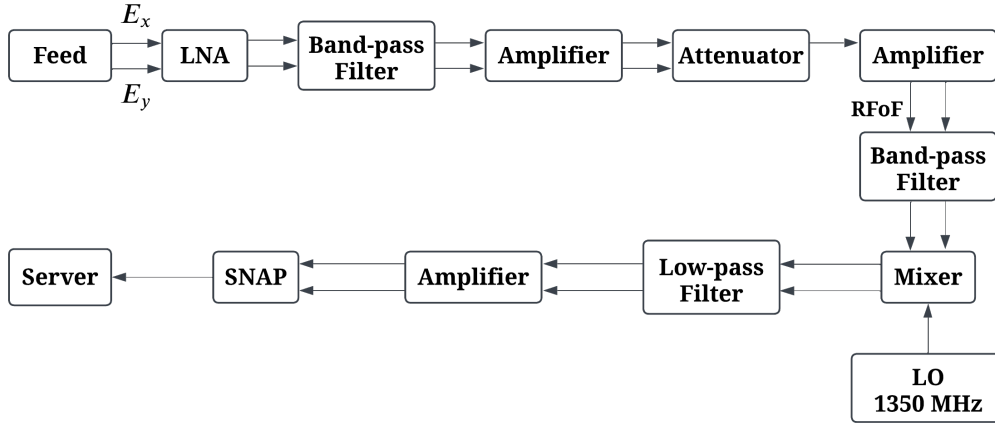


**Figure 3.** Schematic of the LIMBO analogue system. A dual-polarization feed horn captures signals which are amplified and filtered before being transmitted to an indoor processing rack via fibre-optic cabling. Inside, signals are heterodyne mixed, filtered, and further amplified before being digitally sampled on a SNAP board and sent to a local server over a 10-Gb Ethernet connection. The two linear polarizations follow parallel, matched paths on their way to the server.

**Table 1.** Leuschner radio telescope properties.

Parameter	Value
Beam Width	3.43 degrees
Bandwidth	250 MHz
$T_{rx}$ , 1420 MHz	47.34 K
	$5.73 \times 10^{-3}$ K/Jy
Sensitivity	42.2 Jy-ms

### 3.2 RFI Excision

One of the primary challenges faced by LIMBO is the high level of RFI contamination. The Leuschner Observatory’s location in the greater San Francisco Bay Area makes it susceptible to both narrow and broadband interference. Effective mitigation therefore requires careful modelling of the passband and robust excision strategies that suppress RFI “hot spots” while minimizing the risk of inadvertently flagging genuine FRB signals. Although LIMBO’s nominal passband extends from 1.39–1.60 GHz, we restrict our analysis to the cleaner 1.39–1.52 GHz range, excluding frequency regions persistently contaminated by RFI. Bandpass modelling, RFI excision, initial detections, and FRB searches are therefore performed only within this restricted band.

To model the LIMBO passband, we use DPSS Approximate lazY filtEriNg of foregroUnds (DAYENU) (Ewall-Wice et al. 2021). Applied to a time-averaged spectrum, this filter produces a smooth spectral model of the passband. As illustrated in Figure 5, the DPSS filter excludes clock lines, RFI spikes, and other narrow spectral features, yielding a clean model of the underlying passband response.

For each data file, smoothed estimates of  $T_{sys}$  are derived by applying DPSS filters in time and frequency to auto-correlation spectra. From these, thermal noise estimates for each channel are modelled according to the radiometer equation,

$$T_{rms} = \frac{T_{sys}}{\sqrt{\Delta\nu\tau}}$$

where  $T_{rms}$  is the residual (root-mean-squared) noise temperature,  $T_{sys}$  is the (frequency-dependent) system temperature,  $\Delta\nu$  is the width of a frequency channel, and  $\tau$  is the integration time.

For each time–frequency bin, we compute a Z-score relative to this smooth noise model. We then sum the Z-scores across frequency to obtain an aggregate Z-score as a function of time. After subtracting the median, we compute the median absolute deviation (MAD) of the distribution and flag outlying time integrations using a  $4\times$  MAD threshold.

This procedure flags short bursts of excess power while preserving highly dispersed pulses, which distribute power over longer durations and therefore elevate both the median Z-score and MAD sufficiently to avoid rejection, even when per-bin Z-scores are large. Finally, after flagging time–frequency bins, we inpaint flagged data with Gaussian noise consistent with the frequency-dependent noise model to produce detrended, RFI-excised output data. This process is illustrated in Figure 6.

### 3.3 Initial Detection: Searching for FRBs

The initial detection pipeline is illustrated in Figure 7. While both power and voltage spectra are recorded simultaneously, initial detections are performed exclusively using power spectra; each power spectrum file is processed by a Jupyter notebook–based processing template that de-trends, calibrates, flags RFI, inpaints, and dedisperses the spectra. The notebook generates diagnostic plots that allow the observer to quickly evaluate whether a file contains candidate pulses. A new per-file notebook is created and executed each time a power spectrum file is written. The total processing time per file is shorter than the file buffering time, enabling real-time detection.

For sources with known DMs, LIMBO performs dedispersion directly at the reported values. However, for sources with unknown DMs, LIMBO can also conduct blind DM searches using a custom implementation of the Fast Dispersion Measure Transform (FDMT) algorithm (Zackay & Ofek 2017). Implemented in Cython,  $FDMT_{LIMBO}$  is a fully coherent dedispersion algorithm with computational complexity  $N_t N_f \log(N_t) \log(N_f)$ , where  $N_t$  and  $N_f$  denote the number of time and frequency bins, respectively.

We find that  $FDMT_{LIMBO}$  runs approximately twice as fast as the original implementation (Figure 8) on a 4.05 GHz Apple M3 processor, enabling coherent dedispersion of candidate pulses in real time without GPU acceleration. For a data matrix with 2048 frequency channels and 4096 spectra—typical of LIMBO’s power spectrum

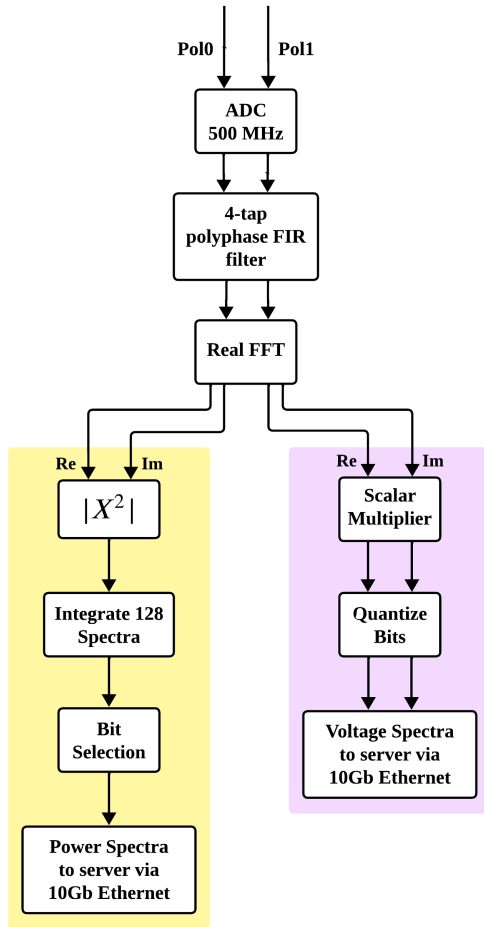


**Figure 4.** Schematic of the LIMBO digital signal processing system. Analogue signals are digitized by dual 8-bit, 500 MHz ADCs on a SNAP board and processed in real time by the onboard Kintex-7 FPGA, the design of which is based upon that of the DSA-10 (Kocz et al. 2019). A polyphase filter bank converts time-domain data into 2048 frequency channels, which are split into parallel power and voltage streams. Power spectra are integrated and down-sampled before transmission to a local server, while voltage spectra are quantized and streamed with high time resolution. Both streams use 10-Gb Ethernet with the HASHPIPE protocol.

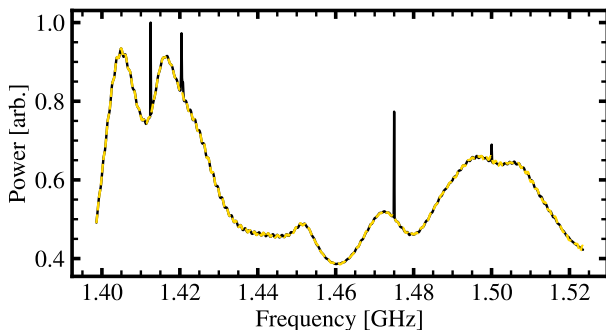


**Figure 5.** Modelling of Leuschner’s bandpass using DPSS filters. The black curve is an uncalibrated Cygnus A spectrum with arbitrary units, time-averaged over  $\sim 28$  s. A DPSS filter excises clock-lines, RFI, and narrow spectral features, yielding a smoothed passband model (dashed yellow).

files—the algorithm completes a full dedispersion in  $\sim 0.26$  s, outputting the measured DM of any detected pulses. An example input and output of  $\text{FDMT}_{\text{LIMBO}}$  is shown in Figure 9.

Dedispersed events exceeding a Z-score significance threshold of 5.5 trigger a file-save response, prompting data dumps from the voltage ring buffer. The threshold of 5.5 was selected as the lowest value that avoids overwhelming the system with spurious candidate pulses. Each saved voltage dataset is subsequently reprocessed through a similar pipeline to confirm the pulse detection. The availability of voltage data enables more detailed analyses of confirmed FRB candidates.

## 4 COMMISSIONING

### 4.1 Signal Injection

During the development stages, we track the progress of the LIMBO system through manual dispersed pulse injection into Leuschner’s antenna. Using a Raspberry Pi 4 paired with a Programmed Test Sources (PTS) frequency synthesizer, we manually inject signals in the form of a continuous wave, a linear frequency sweep, or a quadratic sweep designed to mimic a dispersed FRB pulse. These controlled injections allowed us to test the full signal-recovery pipeline, verify end-to-end performance, and iteratively refine system components before moving on to astrophysical targets.

### 4.2 Giant Crab Pulses

In addition to controlled synthetic tests, we used the Crab Pulsar (PSR B0531+21) as a natural calibration source to validate LIMBO’s performance during observing runs. Giant Crab Pulses (GCPs) mimic FRBs closely enough to test all stages of the system, including the initial detection pipeline, triggered voltage dumps, data recording, and calibration routines under realistic sky conditions.

An example detection is shown in Figure 10, where LIMBO recorded a GCP with a measured dispersion measure of  $56.88 \pm 0.01 \text{ pc} \cdot \text{cm}^{-3}$ , consistent with the established value for the Crab Pulsar (Lyne et al. 1993; McKee et al. 2018; Lewandowska et al. 2022). Using the higher time resolution provided by the voltage data, we were able to resolve the pulse profile in detail. The event yielded a fluence of  $66.8 \pm 6.3 \text{ kJy} \cdot \text{ms}$ , an SNR of 21.46, and a pulse width of  $32.77 \mu\text{s}$ , all consistent with published measurements of other GCPs (Karuppusamy et al. 2010; Bera & Chengalur 2019; Majid et al. 2011).

These detections demonstrate that LIMBO can reliably capture and characterize dispersed astrophysical signals, validating the system performance in FRB searches.

## 5 TENTATIVE FRB DETECTIONS

### 5.1 Targets

Using the McGill magnetar catalogue<sup>3</sup> (Olausen & Kaspi 2014), we determine that 22 of the 30 known Galactic magnetars are observable by the Leuschner Radio Observatory. The characteristics of these observable magnetars and the amount of time each of these sources are visible to the Leuschner Radio Observatory is given in Table 2. This roughly represents the maximum amount of time each source

<sup>3</sup> <http://www.physics.mcgill.ca/~pulsar/magnetar/main.html>

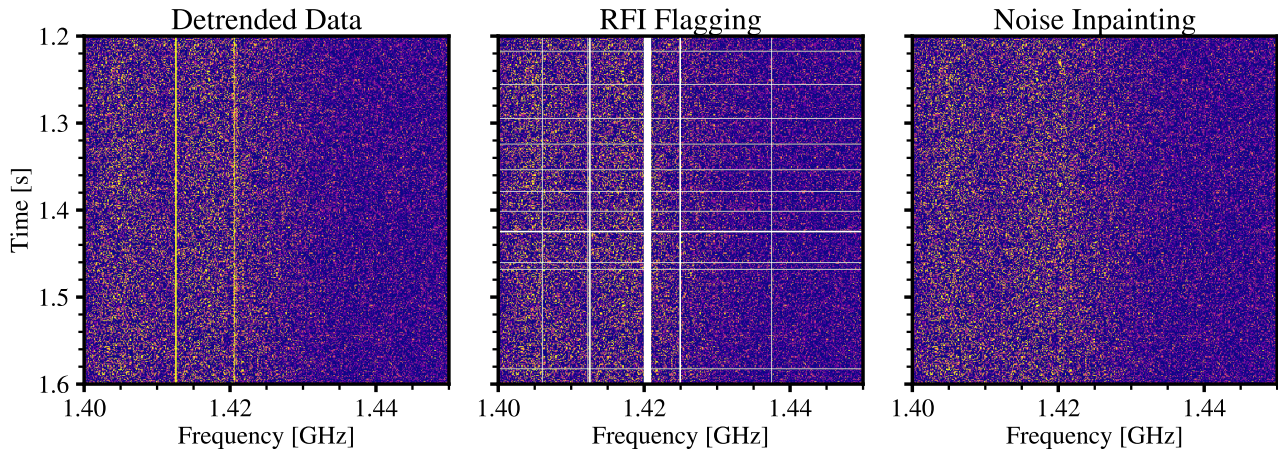


**Figure 6.** The central components of the LIMBO RFI excision pipeline, zoomed in time and frequency range for visual clarity. The left panel shows the data after it has been detrended according to our time and frequency-dependent models. The central panel shows, in white, all the time and frequency channels that were flagged for removal. The right panel contains inpainted Gaussian noise where time and frequency channels were removed.

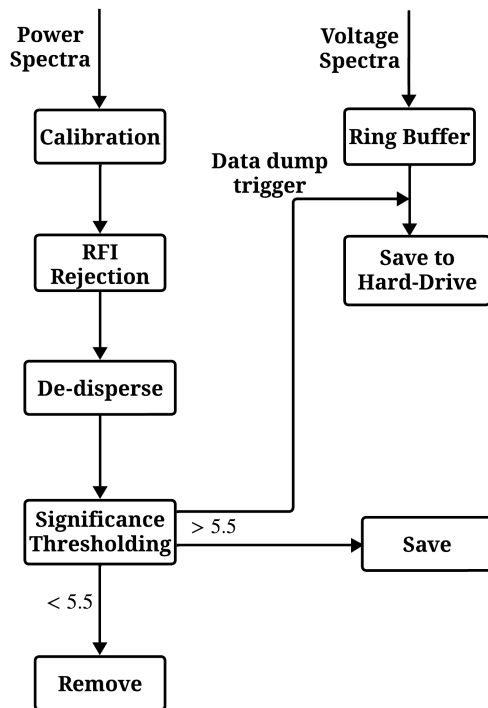


**Figure 7.** LIMBO’s detection pipeline. The SNAP board outputs both voltage and power spectra. Initial detections are done using power spectra (left-hand side) using our real-time processing notebook template, which calibrates and dedisperses the data before searching for candidates. On the right side, voltage data is buffered until a detection is made, at which point both the power and voltage data are saved to hard-drive.

could be targeted on any given day. This table, combined with reports of FRB activity from any of these magnetars, informs our observing strategy.

## 5.2 Observations of SGR 1935+2154

Thus far, LIMBO observations have focused on the Galactic magnetar SGR 1935+2154 because it is a known repeating FRB source with

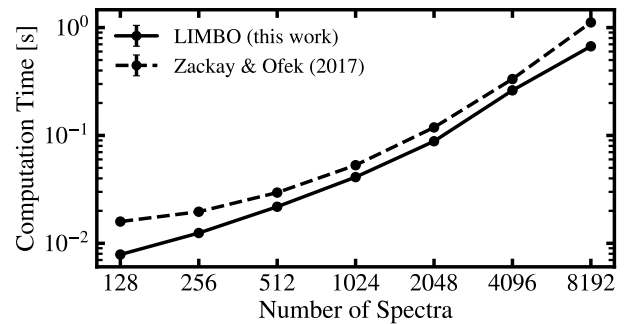


**Figure 8.** A comparison of the original Zackay & Ofek (2017) FDMT algorithm’s run-times versus that of FDMT<sub>LIMBO</sub>. Each version was run on a 4.05 GHz Apple M3 processor. Varied as a function of the number of spectra, each dataset contained a constant 2048 frequency channels. The points correspond to the average run-time measured when sampled 100 times. The error bars indicate the standard deviation on that sample. These run-times show that the LIMBO implementation of the FDMT algorithm can dedisperse data up to 2× faster than the original 2017 implementation, regardless of the number of spectra.

a well-characterized dispersion measure (Bochenek et al. 2020b; Zhang et al. 2020; Kirsten et al. 2021; Zhu et al. 2023; Dong & Chime/Frb Collaboration 2022; Huang et al. 2022; Pearlman & Chime/Frb Collaboration 2022). Between May and August 2023, we conducted a total of 833 hours of follow-up observations of this source.

Candidate FRBs in this dataset are identified through statistical thresholding combined with visual inspection of spectra. As outlined in Section 3.3, we evaluate each file’s significance against a detection threshold to assess the likelihood of it containing an FRB. In the absence of systematics, the distribution of measured Z-scores would follow a standard normal distribution. In practice, however, imperfect RFI excision and residual systematics distort the distribution, shifting the mean toward positive values and inflating the reported significance. Figure 11 shows a histogram of the maximum measured significance per LIMBO file, illustrating this bias.

We choose the most significant event within each file to evaluate as an FRB candidate. All detections are therefore evaluated against an extreme value distribution (EVD) expected from Gaussian noise.

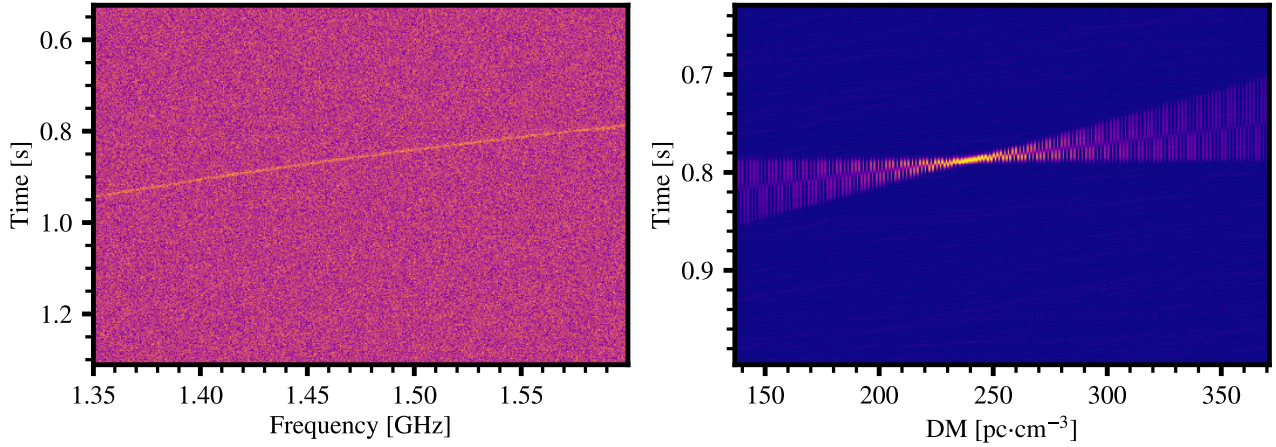


**Figure 9.** *Top:* A computer simulated, dispersed pulse of width 2.12 ms and dispersion measure of  $240 \text{ pc/cm}^3$  sweeping across the LIMBO observing band. A power spectra as a function of time and frequency serves as the input to the FDMT algorithm. *Bottom:* The output of the  $\text{FDMT}_{\text{LIMBO}}$  algorithm. The dispersion measure transform matrix is a function of dispersion measure and time, where the maximum reads the measured DM (in this case,  $240.82 \text{ pc/cm}^3$ ) and the time when the pulse enters the band.

**Table 2.** 22 of the 30 known Galactic magnetars are observable from the Leuschner Radio Observatory. Listed are their daily visibilities, dispersion measures (DMs), and characteristic ages.

Source	LIMBO visibility [hrs/day]	DM [ $\text{pc cm}^{-3}$ ] <sup>a</sup>	$\tau_c$ [kyr] <sup>b</sup>	Ref.
4U 0142+61	18.5	27	68	1, 2
SGR 0418+5729	17.0	50 (5)	$3.6 \times 10^4$	1, 2
SGR 0501+4516	14.4	...	15	2
SGR J1745-2900	4.8	1778 (3)	4.3 – 9.7	1, 2
SGR 1806-20	6.6	~ 750	0.16 – 1.45	2, 3
XTE J1810-197	6.8	178 (5)	8.4 – 20	1, 2
Swift J1818.0-1607	7.4	706 (4)	0.47	1, 4
Swift J1822.3-1606	7.4	...	1600 – 6400	2
SGR 1833-0832	8.4	...	34	2
Swift J1834.9-0846	8.4	...	4.9	2
1E 1841-045	8.9	~ 746	4.5	2, 3, 5
3XMM J185246.6+003317	9.5	...	> 1300	2
SGR 1900+14	10.4	281.4 (0.9)	0.46 – 1.3	2, 6
SGR 1935+2154	11.6	332.7206 (9)	3.6	1, 2
1E 2259+586	17.4	79	230	1, 2
SGR 0755-2933	4.6	...	...	...
SGR 1801-23	6.2	...	...	...
SGR 1808-20	6.6	...	...	...
AX J1818.8-1559	7.4	...	...	...
AX J1845.0-0258	9.1	...	...	...
SGR 2013+34	13.0	...	...	...
PSR J1846-0258	9.1	...	0.73	2

<sup>a</sup> DM values are only populated when there is a published radio pulsar detection and a catalogued DM.

<sup>b</sup> Characteristic (dipole spin-down) age.

References: (1) Olausen & Kaspi (2014); (2) Beniamini et al. (2019); (3) Lazarus et al. (2012); (4) Hu et al. (2020); (5) Younes et al. (2025); (6) Shitov (1999).

Any systematic shift of the observed EVD relative to the simulated distribution reflects the combined effects of residual RFI and other unmitigated systematics.

To quantify this effect, we conducted a ~ 6 hr calibration run slightly off-target from SGR 1935+2154. This dataset characterizes the instrument's triggering environment in the absence of genuine FRBs. From this analysis, we find that unflagged RFI inflates measured Z-scores by approximately 0.25. We therefore subtract this offset from all candidate events to obtain corrected significance values.

We then examine the shape of the calibrated EVD in greater detail.

At high significance levels, the observed tail of the distribution is systematically suppressed compared to expectations, with events at  $Z > 4.5$  occurring at rates ~ 10% below the simulated Gaussian prediction. This deficit may be the result of over-flagging within the LIMBO RFI excision pipeline. However, comparisons of flagged and unflagged distributions show that only ~ 1% of the suppression can be accounted for by differences in flagged channels, suggesting that a more detailed noise analysis and stronger characterization of the LIMBO pipeline is required. We acknowledge that this biases us towards under-reporting the significance of high-Z results, but for this work we do not attempt to apply additional corrections.

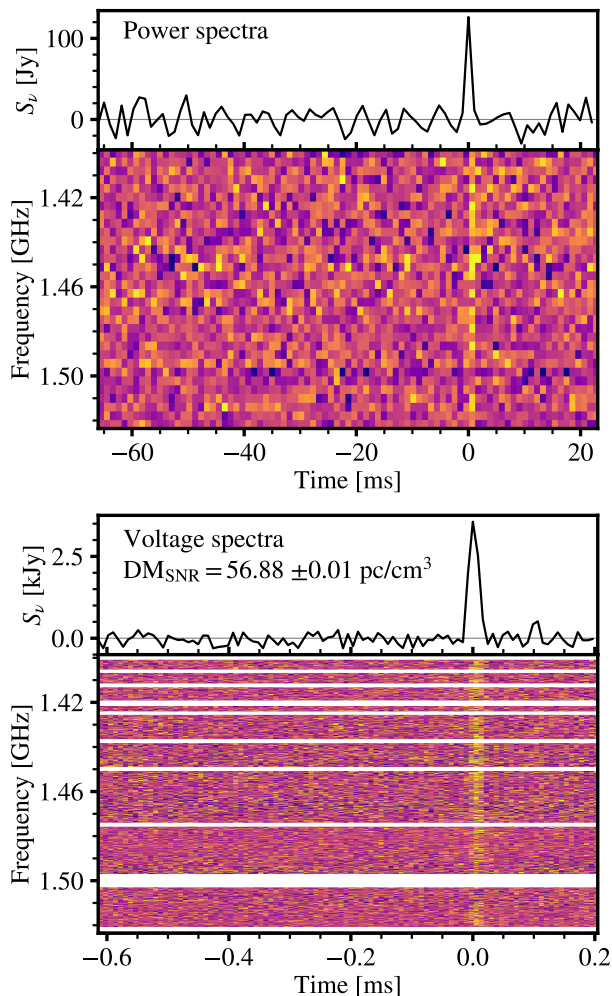


**Figure 10.** Detection of a giant radio pulse from the Crab Pulsar using LIMBO. *Top:* The power spectra of GCP230707 as it is seen by LIMBO’s initial detection pipeline. The pulse was dedispersed to the known DM of the Crab pulsar ( $56.7 \text{ pc}\cdot\text{cm}^{-3}$ ) for detection purposes. *Bottom:* Corresponding voltage data of GCP230707. The pulse was dedispersed such that the SNR was maximized, giving a measured DM of  $56.88 \pm 0.01 \text{ pc}\cdot\text{cm}^{-3}$ . Flagged frequency channels are masked out in white. In each figure, the top panel shows the frequency-averaged flux density of the pulse as a function of time, while the bottom panel displays the time and frequency-domain profile.

After applying an offset correction derived from the off-source calibration run, the measured EVD aligns much more closely with the simulations. This corrected Z-score is used for interpretation within the statistical framework assumed by our pipeline.

By the central limit theorem, the right tail of an EVD is well-approximated by a Gaussian distribution, particularly at Z-scores above the trigger threshold. In Figure 12 (left), we directly compare the calibrated EVD of observations to an ensemble of simulations, while Figure 12 (right) presents the cumulative distribution of maximum Z-scores. A Gaussian is fit to the average of the simulated distributions. The cumulative plot reveals that the observed tail is suppressed relative to the Gaussian fit, with shaded regions marking the 68%, 95%, and 99.7% confidence intervals derived from repeated Poisson resampling. Despite this suppression, we find a clear excess of events over the simulated expectation in bins with  $Z \geq 5.8$ .

We select all events with significance  $\geq 5.6$  for further analysis, yielding 24 candidate bursts. We expect false positives from

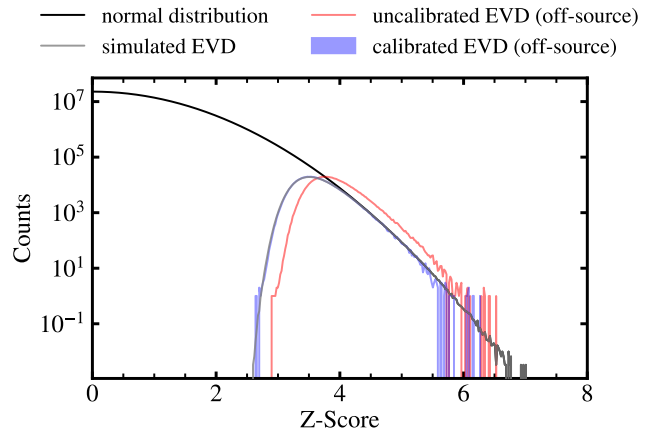


**Figure 11.** Histogrammed significances of an off-SGR 1935+2154 observing run plotted against the average of 100 simulated trials. The red curve represents the uncalibrated EVD obtained from the observing run. Subtracting the difference between the means of the simulated EVD and uncalibrated EVD gives us a calibrated EVD for SGR 1935+2154 (blue). The calibrated EVD is compared to that expected by Gaussian noise (grey). Overplotted in black is a normal distribution, illustrating that the right tail of an EVD can be well approximated by a Gaussian distribution.

Gaussian noise alone to be rare ( $P(Z \geq 5.6) = 1 \times 10^{-8}$ ). Each candidate’s power spectrum is visually inspected and compared to expectations for FRB-like signatures. Of these 24 events, we classify 12 as plausible FRBs, 7 as spurious events attributable to RFI, and 3 as a combination of RFI and FRB-like behaviour (see Appendices A and B). Candidate FRBs are presented in Figure A1, with pulse properties listed in Table 3. Events highlighted in bold represent the most secure identifications, supported by both high statistical significance and clean spectral-temporal profiles consistent with FRBs. The measured DMs of these candidates are consistent with previously published values for SGR 1935+2154.

Figure B1 (top) shows example spectra representative of the 7 events classified as RFI-induced false-positives. In contrast to those in Figure A1, the RFI-induced events show broad or variable time and frequency structures, making them easy to rule out as FRBs.

Sometimes, genuine low-SNR bursts can be partially or fully obscured in files with RFI. As described in Section 3, spectra are flagged, dedispersed, and inpainted across flagged channels to stabilize downstream statistics. In RFI-heavy intervals, this procedure introduces a sharp visual boundary between “clean” (inpainted) and “dirty” (unflagged but contaminated) regions in the dynamic spectrum. After dedispersion, this boundary shifts, producing the negatively sloped feature seen clearly in RFI230524 (Figure B1).

If an FRB overlaps such boundaries, only a subset of channels may retain astrophysical signal, while others are masked and replaced with Gaussian noise. This yields candidate FRBs that appear to occupy only part of LIMBO’s passband. We observe this behaviour in 3 of the 24 files (Figure B1 (bottom)). Although these events exhibit pulses with DMs consistent with SGR 1935+2154, heavy contamination from RFI and inpainting prevents us from assessing their FRB candidacy with confidence. At present, LIMBO’s search pipeline does not attempt a dedicated recovery of such “hidden” FRBs, and they are excluded from our secure sample.

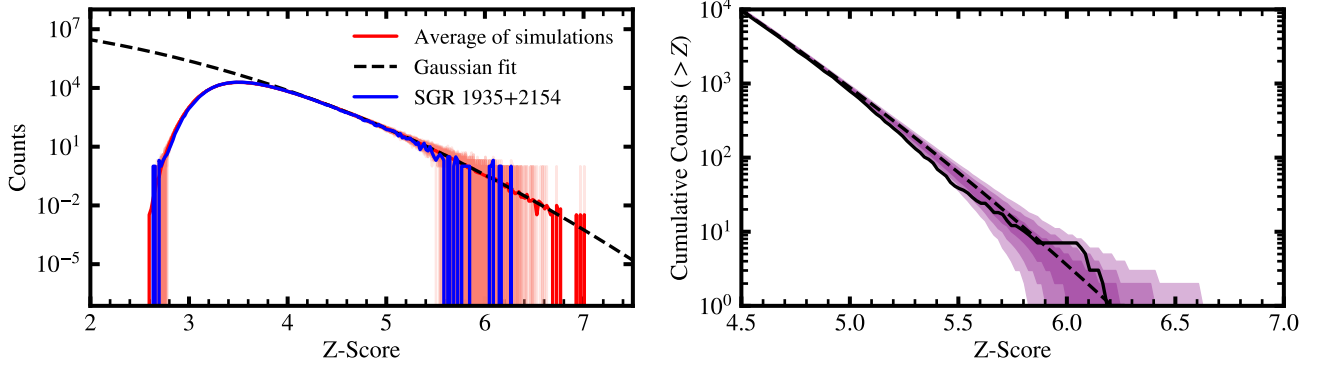


**Figure 12.** *Left:* EVDs of the SGR 1935+2154 observing run (blue) and 100 simulations (pink). The average EVD of these simulations is plotted in red. A Gaussian was fit to the tail of the averaged EVD (black dashed). *Right:* A cumulative distribution of the SGR 1935+2154 observing run (black, solid) plotted against the same Gaussian fit to the average of the simulations in the left panel (black, dashed). The purple (from darkest to lightest) represent the 68%, 95%, and 99.7% confidence intervals drawn from a Poisson distribution sampled 300 times. The suppression of the distribution’s tail from the Gaussian fit is the result of unmitigated systematics.

**Table 3.** Candidate FRBs detected by the LIMBO system between May and August 2023, along with their measured pulse properties. Dispersion measures are obtained by maximizing the pulse SNR. Fluence uncertainties are calculated over a time window centred on the burst that is shorter than the full file duration, ensuring that possible RFI elsewhere in the file does not bias the noise statistics for the burst. Candidate names shown in bold mark the bursts judged most reliable after visual inspection of their power spectra.

Name	DM±0.01 [pc/cm <sup>3</sup> ]	Fluence [Jy·ms]	SNR	Z-score
<b>LIMBO230524A</b>	330.47	79 ± 15	6.12	5.85
<b>LIMBO230524B</b>	329.70	80 ± 13	6.13	5.85
<b>LIMBO230526</b>	333.49	105 ± 17	5.99	5.71
<b>LIMBO230527A</b>	331.21	79 ± 13	5.90	5.61
<b>LIMBO230527B</b>	330.82	75 ± 13	5.94	5.66
<b>LIMBO230608</b>	332.13	78 ± 13	6.05	5.76
<b>LIMBO230613</b>	334.13	80 ± 13	6.46	6.17
LIMBO230617	332.93	74 ± 14	6.10	5.81
<b>LIMBO230708</b>	334.06	82 ± 13	6.51	6.21
<b>LIMBO230720</b>	330.41	79 ± 13	6.09	5.79
LIMBO230721	334.41	68 ± 12	6.32	6.04
<b>LIMBO230810</b>	332.55	201 ± 33	5.91	5.63

### 5.3 SGR 1935+2154 Rates

Our goal is to estimate the annual event rate from SGR 1935+2154 as a function of fluence,  $R(\geq \mathcal{F})$ . It is possible that our sample contains false-positives. The false-positive expectation number can be determined by integrating the tail of the cumulative distribution shown in Figure 12. However, this distribution is a function of Z-score and systematics in our Z-scores make it difficult to translate expectations from that distribution into fluence space.

To address this, we average fluence errors for each burst to establish an approximate relationship between an  $n\sigma$  event and its corresponding fluence. This yields  $1\sigma \approx 13 \text{ Jy} \cdot \text{ms}$ . LIMBO230810 is excluded from this average because its noise statistics are noticeably different from the rest in the sample. Using this relation, we set the first of our fluence bins at the  $5\sigma$  level ( $\mathcal{F} = 65 \text{ Jy} \cdot \text{ms}$ ) and logarithmically space the subsequent bins to reduce biases from small-number statistics.

The expected number of false-positives in a given fluence bin is obtained by integrating the Gaussian tail,

$$N_{\text{false}}(b_i, b_{i+1}) = \frac{N_{\text{trials}}}{2} \left[ \text{erf} \left( \frac{b_{i+1}}{\sqrt{2}\sigma} \right) - \text{erf} \left( \frac{b_i}{\sqrt{2}\sigma} \right) \right]$$

where  $b_i$  and  $b_{i+1}$  are the lower and upper fluence edges of the bin, respectively, and  $\sigma = 13 \text{ Jy} \cdot \text{ms}$ .

Applying this formulation, 11 bursts fall in the  $\mathcal{F} \geq 65 \text{ Jy} \cdot \text{ms}$  bin and 1 burst in the  $\mathcal{F} \geq 130 \text{ Jy} \cdot \text{ms}$  bin. At most 1 spurious event is expected in the first bin and none in the second. These values are subtracted from the observed counts before rate estimation.

Sampling from a Poisson distribution then yields  $R(\geq 65 \text{ Jy} \cdot \text{ms}) = 112.3^{+81.3}_{-54.5} \text{ yr}^{-1}$  and  $R(\geq 130 \text{ Jy} \cdot \text{ms}) = 17.7^{+40.8}_{-15.1} \text{ yr}^{-1}$ , with uncertainties corresponding to 95% confidence intervals.

Figure 13 compares these rates to those inferred from other well-documented SGR 1935+2154 FRBs (Bochenek et al. 2020b; Kirsten et al. 2021; Giri et al. 2023). As was done for LIMBO, uncertainties in the rates for Kirsten et al. (2021) and Giri et al. (2023) are derived by sampling their respective Poisson likelihoods. A power-law model is fit to the cumulative rate-fluence distribution using the Markov chain Monte Carlo (MCMC) sampler emcee (Foreman-Mackey et al. 2013), yielding a slope of  $\alpha = -0.60^{+0.24}_{-0.28}$ , where uncertainties correspond to the 95% highest-density interval.

We show two representations of the 1.5 MJy · ms burst detected by STARE2 (Bochenek et al. 2020b). The first corresponds to a population-averaged rate (solid pink), which accounts for the look-elsewhere effect arising from STARE2’s all-sky monitoring of multiple Galactic magnetars over an extended observing time. In this case, the effective observing time is obtained by summing the visibility-weighted observing times over the entire known Galactic magnetar

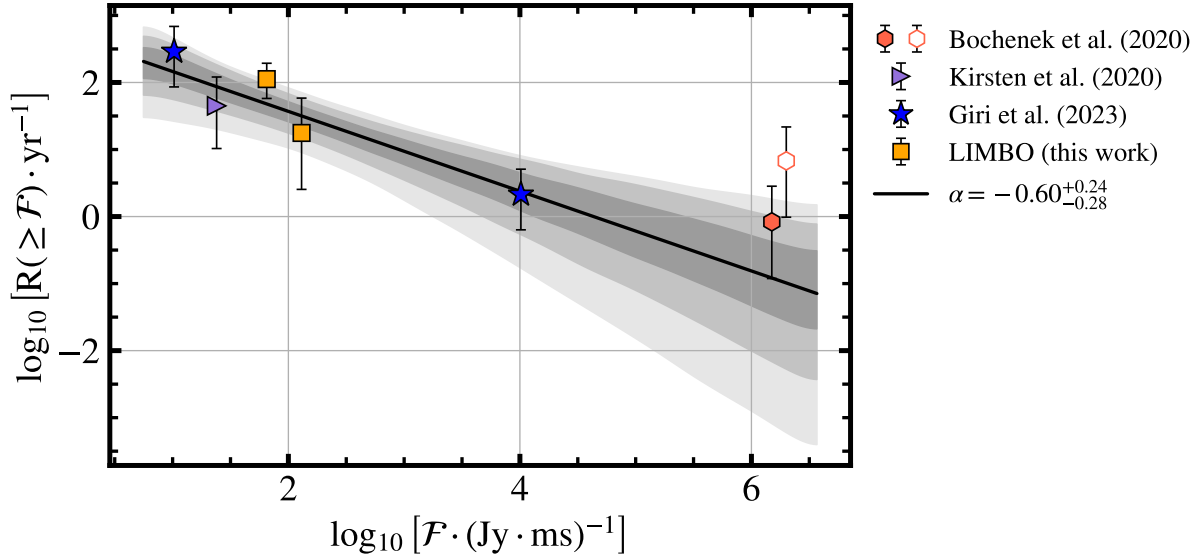


**Figure 13.** Cumulative burst rate as a function of fluence for FRBs associated with SGR 1935+2154. Rates derived from [Kirsten et al. \(2021\)](#) and [Giri et al. \(2023\)](#) are shown alongside the LIMBO results from this work, with uncertainties derived from their respective Poisson likelihoods. Two representations of the STARE2 ([Bochenek et al. 2020b](#)) 1.5 Jy · ms burst are shown: a population-averaged rate (solid pink), which accounts for look-elsewhere-effect corrections and marginalizes the uncertainty on the number of unknown Galactic magnetars, and a source-conditioned rate (white marker with pink outline), accounting only for the effective observing time in which SGR 1935+2154 was visible to STARE2 and Poisson uncertainty alone. The population-averaged marker is offset slightly in fluence for visual clarity. All rate uncertainties correspond to a 95% confidence interval. The solid black line shows the line of best fit for the power-law model to the cumulative rate-fluence distribution, with a slope of  $\alpha = -0.60^{+0.24}_{-0.28}$  (95% CI). The fit excludes the source-conditioned STARE2 rate. The shaded regions, from dark to light gray, correspond to the 68%, 95%, and 99.7% highest-density intervals of the model posterior, respectively.

population. The inferred rate is further marginalized over uncertainty in the number of currently unknown Galactic magnetars by weighting STARE2’s Poisson likelihood (modeled as a Gamma distribution) with an exponential prior with a scale of  $\sigma = 1$  on the number of unseen magnetars. We find that variations in the scale ( $\sigma = 0.01 - 10$ ) alter the inferred power-law slope by less than 4%, and therefore do not change our conclusions.

For comparison, we also show a source-conditioned rate using only the effective observing time during which SGR 1935+2154 itself was visible to STARE2 (white marker with pink outline). This point reflects Poisson uncertainty alone without additional population-averaging or look-elsewhere corrections. Although the STARE2 burst is associated with SGR 1935+2154, the detection resulted from an untargeted, all-sky experiment. The inferred rate therefore reflects a draw from the Galactic magnetar population rather than a source-conditioned rate. As a result, only the population-averaged rate and corresponding likelihood is used in the rate-fluence power-law fit.

As discussed in Section 5.2 and Appendix B, three events with  $Z \geq 5.6$  exhibit FRB-like features but are heavily contaminated by RFI. If we treat these events as candidate FRBs, the inferred rate for SGR 1935+2154 shows a modest increase to  $R(\geq 65 \text{ Jy} \cdot \text{ms}) = 143.8^{+90.1}_{-63.3} \text{ yr}^{-1}$ . There is no change in  $R(\geq 130 \text{ Jy} \cdot \text{ms})$ . Moreover, the consideration of these “hidden” bursts changes the inferred power-law slope,  $\alpha$ , by less than 5%.

## 6 CONCLUSION

The Long-Integration Magnetar Burst Observatory (LIMBO) is a real-time radio transient detection pipeline specifically designed to conduct directed, long-term observations of Galactic magnetars to detect and characterize fast radio bursts (FRBs). LIMBO is currently deployed on the UC Berkeley Leuschner Radio Observatory’s 4.3-m

radio dish, equipped with a dual-polarization feed horn and operating with a 250 MHz passband centred at 1475 MHz. A real-time processing pipeline searches for dispersed transients in the combined polarizations using a modified Fast Dispersion Measure Transform (FDMT) algorithm for coherent dedispersion of bursts, and triggers a dump of voltage data to drive when a candidate FRB is detected. Using a combination of on-sky calibrations, synthetic signal-injection and recovery tests, and the successful detection of giant pulses from the Crab Pulsar, we validate LIMBO’s sensitivity to radio transients with fluences  $\geq 43 \text{ Jy} \cdot \text{ms}$ . Its sensitivity to faint Galactic FRBs and capacity to carry-out  $\sim 10^4$  hours of follow-up observations allow LIMBO to explore an otherwise untouched parameter space in FRB detections (Figure 1).

Between May and August 2023, LIMBO conducted 833 hrs of follow-up of Galactic magnetar SGR 1935+2154. We identify 12 bursts tentatively classified as candidate FRBs, yielding inferred rates of  $R(\geq 65 \text{ Jy} \cdot \text{ms}) = 112.3^{+81.3}_{-54.5} \text{ yr}^{-1}$  and  $R(\geq 130 \text{ Jy} \cdot \text{ms}) = 17.7^{+40.8}_{-15.1} \text{ yr}^{-1}$ . These bursts are compared with other detected FRBs from SGR 1935+2154, and a cumulative rate-fluence power-law slope of  $\alpha = -0.60^{+0.24}_{-0.28}$  is obtained (Figure 13).

Beyond expanding the census of Galactic FRBs, LIMBO provides a critical step toward connecting burst phenomenology with the underlying emission physics. Long-duration, directed monitoring of a single, well-characterized source enables constraints on burst clustering, fluence distributions, polarization properties, and temporal correlations with high-energy activity-observables that are difficult to access in wide-field, discovery-driven surveys. The ability to trigger voltage dumps further allows for high-time-resolution studies of burst substructure, coherence, and polarization evolution, all of which encode information about the emission region and mechanism.

In this sense, LIMBO complements large population surveys by shifting the emphasis from detection rates alone to physically moti-

vated characterization of individual sources. As such, LIMBO helps bridge the gap between cosmological FRB statistics and source-resolved studies, providing a pathway toward distinguishing between competing emission models and clarifying the role of magnetars as FRB progenitors.

Future work with LIMBO will focus on detailed analysis of voltage data for the candidates presented in this work, alongside continued searches for and characterization of new candidates in ongoing follow-up observations of SGR 1935+2154 and other Galactic magnetars.

## ACKNOWLEDGMENTS

D.M. acknowledges Matt Dexter and Christian Hellum Bye for early guidance and valuable discussions, particularly regarding the design of the LIMBO instrument and development of the transient detection pipeline. D.M. further thanks Padma Venkatraman for valuable discussion and advice regarding statistical analysis.

## DATA AVAILABILITY

Calibrating data for SGR 1935+2154 statistics as well as data containing the 24 events analysed for candidate FRBs can be found at <https://doi.org/10.5281/zenodo.18870723>. The LIMBO processing pipeline and telescope control software can be found at <https://github.com/AaronParsons/limbo>. Data recording backends used for LIMBO are found at [https://github.com/liuweiseu/limbo\\_recorder/tree/auto\\_files](https://github.com/liuweiseu/limbo_recorder/tree/auto_files), while control of the LIMBO SNAP board is found at [https://github.com/liuweiseu/limbo\\_scripts](https://github.com/liuweiseu/limbo_scripts).

## REFERENCES

- Baars, J. W. M., Genzel, R., Pauliny-Toth, I. I. K., & Witzel, A., 1977. The absolute spectrum of Cas A: an accurate flux density scale and a set of secondary calibrators., *A&A*, **61**, 99–106.
- Bailes, M., Jameson, A., Flynn, C., Bateman, T., Barr, E. D., Bhandari, S., Bunton, J. D., Caleb, M., Campbell-Wilson, D., Farah, W., Gaensler, B., Green, A. J., Hunstead, R. W., Jankowski, F., Keane, E. F., Krishnan, V. V., Murphy, T., O’Neill, M., Osłowski, S., Parthasarathy, A., Ravi, V., Rosado, P., & Temby, D., 2017. The UTMOST: A Hybrid Digital Signal Processor Transforms the Molonglo Observatory Synthesis Telescope, *Publ. Astron. Soc. Australia*, **34**, e045.
- Bannister, K. W., Shannon, R. M., Macquart, J.-P., Flynn, C., Edwards, P. G., O’Neill, M., Osłowski, S., Bailes, M., Zackay, B., Clarke, N., D’Addario, L. R., Dodson, R., Hall, P. J., Jameson, A., Jones, D., Navarro, R., Trinh, J. T., Allison, J., Anderson, C. S., Bell, M., Chippendale, A. P., Collier, J. D., Heald, G., Heywood, I., Hotan, A. W., Lee-Waddell, K., Madrid, J. P., Marvil, J., McConnell, D., Popping, A., Voronkov, M. A., Whiting, M. T., Allen, G. R., Bock, D. C.-J., Brodrick, D. P., Cooray, F., DeBoer, D. R., Diamond, P. J., Ekers, R., Gough, R. G., Hampson, G. A., Harvey-Smith, L., Hay, S. G., Hayman, D. B., Jackson, C. A., Johnston, S., Koribalski, B. S., McClure-Griffiths, N. M., Mirtschin, P., Ng, A., Norris, R. P., Pearce, S. E., Phillips, C. J., Roxby, D. N., Troup, E. R., & Westmeier, T., 2017. The Detection of an Extremely Bright Fast Radio Burst in a Phased Array Feed Survey, *ApJ*, **841**(1), L12.
- Beloborodov, A. M., 2020. Blast Waves from Magnetar Flares and Fast Radio Bursts, *ApJ*, **896**(2), 142.
- Beniamini, P., Hotokezaka, K., van der Horst, A., & Kouveliotou, C., 2019. Formation rates and evolution histories of magnetars, *MNRAS*, **487**(1), 1426–1438.
- Bera, A. & Chengalur, J. N., 2019. Super-giant pulses from the Crab pulsar: energy distribution and occurrence rate, *MNRAS*, **490**(1), L12–L16.
- Bhandari, S., Keane, E. F., Barr, E. D., Jameson, A., Petroff, E., Johnston, S., Bailes, M., Bhat, N. D. R., Burgay, M., Burke-Spolaor, S., Caleb, M., Eatough, R. P., Flynn, C., Green, J. A., Jankowski, F., Kramer, M., Krishnan, V. V., Morello, V., Possenti, A., Stappers, B., Tiburzi, C., van Straten, W., Andreoni, I., Butterley, T., Chandra, P., Cooke, J., Corongiu, A., Coward, D. M., Dhillon, V. S., Dodson, R., Hardy, L. K., Howell, E. J., Jaroenjtitchai, P., Klotz, A., Littlefair, S. P., Marsh, T. R., Mickaliger, M., Muxlow, T., Perrodin, D., Pritchard, T., Sawangwit, U., Terai, T., Tominaga, N., Torne, P., Totani, T., Trois, A., Turpin, D., Niino, Y., Wilson, R. W., Albert, A., André, M., Anghinolfi, M., Anton, G., Ardid, M., Aubert, J.-J., Avgitas, T., Baret, B., Barrios-Martí, J., Basa, S., Belhorma, B., Bertin, V., Biagi, S., Bormuth, R., Bourret, S., Bouwhuis, M. C., Brânzaș, H., Bruijn, R., Brunner, J., Busto, J., Capone, A., Caramete, L., Carr, J., Celli, S., Moursli, R. C. E., Chiarusi, T., Circella, M., Coelho, J. A. B., Coleiro, A., Coniglione, R., Costantini, H., Coyle, P., Creusot, A., Díaz, A. F., Deschamps, A., De Bonis, G., Distefano, C., Palma, I. D., Domi, A., Donzaud, C., Dornic, D., Drouhin, D., Eberl, T., Bojaddaini, I. E., Khayati, N. E., Elsässer, D., Enzenhöfer, A., Ettahiri, A., Fassi, F., Felis, I., Fusco, L. A., Gay, P., Giordano, V., Glotin, H., Gregoire, T., Gracia-Ruiz, R., Graf, K., Hallmann, S., van Haren, H., Heijboer, A. J., Hello, Y., Hernández-Rey, J. J., Höfl, J., Hofestädt, J., Hugon, C., Illuminati, G., James, C. W., de Jong, M., Jongen, M., Kadler, M., Kalekin, O., Katz, U., Kießling, D., Kouchner, A., Kreter, M., Kreykenbohm, I., Kulikovskiy, V., Lachaud, C., Lahmann, R., Lefèvre, D., Leonora, E., Loucatos, S., Marcellin, M., Margiotta, A., Marinelli, A., Martínez-Mora, J. A., Mele, R., Melis, K., Michael, T., Migliozi, P., Moussa, A., Navas, S., Nezir, E., Organokov, M., Pāvālaš, G. E., Pellegrino, C., Perrina, C., Piatelli, P., Popa, V., Pradier, T., Quinn, L., Racca, C., Riccobene, G., Sánchez-Losa, A., Saldaña, M., Salvadori, I., Samtleben, D. F. E., Sanguineti, M., Sapienza, P., Schüssler, F., Sieger, C., Spurio, M., Stolarczyk, T., Taiuti, M., Tayalati, Y., Trovato, A., Turpin, D., Tönnis, C., Vallage, B., Van Elewyck, V., Versari, F., Vivolo, D., Vizzocca, A., Wilms, J., Zornoza, J. D., & Zúñiga, J., 2018. The SURvey for Pulsars and Extragalactic Radio Bursts - II. New FRB discoveries and their follow-up, *MNRAS*, **475**(2), 1427–1446.
- Bochenek, C. D., McKenna, D. L., Belov, K. V., Kocz, J., Kulkarni, S. R., Lamb, J., Ravi, V., & Woody, D., 2020a. STARE2: Detecting Fast Radio Bursts in the Milky Way, *PASP*, **132**(1009), 034202.
- Bochenek, C. D., Ravi, V., Belov, K. V., Hallinan, G., Kocz, J., Kulkarni, S. R., & McKenna, D. L., 2020b. A fast radio burst associated with a Galactic magnetar, *Nature*, **587**(7832), 59–62.
- Caleb, M., Flynn, C., Bailes, M., Barr, E. D., Bateman, T., Bhandari, S., Campbell-Wilson, D., Farah, W., Green, A. J., Hunstead, R. W., Jameson, A., Jankowski, F., Keane, E. F., Parthasarathy, A., Ravi, V., Rosado, P. A., van Straten, W., & Venkatraman, V., 2017. The first interferometric detections of fast radio bursts, *MNRAS*, **468**(3), 3746–3756.
- Champion, D. J., Petroff, E., Kramer, M., Keith, M. J., Bailes, M., Barr, E. D., Bates, S. D., Bhat, N. D. R., Burgay, M., Burke-Spolaor, S., Flynn, C. M. L., Jameson, A., Johnston, S., Ng, C., Levin, L., Possenti, A., Stappers, B. W., van Straten, W., Thornton, D., Tiburzi, C., & Lyne, A. G., 2016. Five new fast radio bursts from the HTRU high-latitude survey at Parkes: first evidence for two-component bursts, *MNRAS*, **460**(1), L30–L34.
- CHIME/FRB Collaboration, Amiri, M., Bandura, K., Berger, P., Bhardwaj, M., Boyce, M. M., Boyle, P. J., Brar, C., Burhanpurkar, M., Chawla, P., Chowdhury, J., Cliche, J.-F., Cranmer, M. D., Cubranic, D., Deng, M., Denman, N., Dobbs, M., Fandino, M., Fonseca, E., Gaensler, B. M., Giri, U., Gilbert, A. J., Good, D. C., Guliani, S., Halpern, M., Hinshaw, G., Höfer, C., Josephy, A., Kaspi, V. M., Landecker, T. L., Lang, D., Liao, H., Masui, K. W., Mena-Parra, J., Naidu, A., Newburgh, L. B., Ng, C., Patel, C., Pen, U.-L., Pinsonneault-Marotte, T., Pleunis, Z., Raffei Ravandi, M., Ransom, S. M., Renard, A., Scholz, P., Sigurdson, K., Siegel, S. R., Smith, K. M., Stairs, I. H., Tendulkar, S. P., Vanderlinde, K., & Wiebe, D. V., 2018. The CHIME Fast Radio Burst Project: System Overview, *ApJ*, **863**(1), 48.

- CHIME/FRB Collaboration, Andersen, B. C., Bandura, K. M., Bhardwaj, M., Bij, A., Boyce, M. M., Boyle, P. J., Brar, C., Cassanelli, T., Chawla, P., Chen, T., Cliche, J.-F., Cook, A., Cubranic, D., Curtin, A. P., Denman, N. T., Dobbs, M., Dong, F. Q., Fandino, M., Fonseca, E., Gaensler, B. M., Giri, U., Good, D. C., Halpern, M., Hill, A. S., Hinshaw, G. F., Höfer, C., Josephy, A., Kania, J. W., Kaspi, V. M., Landecker, T. L., Leung, C., Li, D. Z., Lin, H.-H., Masui, K. W., McKinven, R., Mena-Parra, J., Merryfield, M., Meyers, B. W., Michilli, D., Milutinovic, N., Mirhosseini, A., Münchmeyer, M., Naidu, A., Newburgh, L. B., Ng, C., Patel, C., Pen, U.-L., Pinsonneault-Marotte, T., Pleunis, Z., Quine, B. M., Rafiei-Ravandi, M., Rahman, M., Ransom, S. M., Renard, A., Sanghavi, P., Scholz, P., Shaw, J. R., Shin, K., Siegel, S. R., Singh, S., Smegal, R. J., Smith, K. M., Stairs, I. H., Tan, C. M., Tendulkar, S. P., Tretyakov, I., Vanderlinde, K., Wang, H., Wulf, D., & Zwaniga, A. V., 2020. A bright millisecond-duration radio burst from a Galactic magnetar, *Nature*, **587**(7832), 54–58.
- CHIME/FRB Collaboration, Amiri, M., Andersen, B. C., Bandura, K., Berger, S., Bhardwaj, M., Boyce, M. M., Boyle, P. J., Brar, C., Breitman, D., Cassanelli, T., Chawla, P., Chen, T., Cliche, J.-F., Cook, A., Cubranic, D., Curtin, A. P., Deng, M., Dobbs, M., Dong, F. A., Eadie, G., Fandino, M., Fonseca, E., Gaensler, B. M., Giri, U., Good, D. C., Halpern, M., Hill, A. S., Hinshaw, G., Josephy, A., Kaczmarek, J. F., Kader, Z., Kania, J. W., Kaspi, V. M., Landecker, T. L., Lang, D., Leung, C., Li, D., Lin, H.-H., Masui, K. W., McKinven, R., Mena-Parra, J., Merryfield, M., Meyers, B. W., Michilli, D., Milutinovic, N., Mirhosseini, A., Münchmeyer, M., Naidu, A., Newburgh, L., Ng, C., Patel, C., Pen, U.-L., Petroff, E., Pinsonneault-Marotte, T., Pleunis, Z., Rafiei-Ravandi, M., Rahman, M., Ransom, S. M., Renard, A., Sanghavi, P., Scholz, P., Shaw, J. R., Shin, K., Siegel, S. R., Sikora, A. E., Singh, S., Smith, K. M., Stairs, I., Tan, C. M., Tendulkar, S. P., Vanderlinde, K., Wang, H., Wulf, D., & Zwaniga, A. V., 2021. The First CHIME/FRB Fast Radio Burst Catalog, *ApJS*, **257**(2), 59.
- Chime/Frb Collaboration, Andersen, B. C., Bandura, K., Bhardwaj, M., Boyle, P. J., Brar, C., Cassanelli, T., Chatterjee, S., Chawla, P., Cook, A. M., Curtin, A. P., Dobbs, M., Dong, F. A., Faber, J. T., Fandino, M., Fonseca, E., Gaensler, B. M., Giri, U., Herrera-Martin, A., Hill, A. S., Ibik, A., Josephy, A., Kaczmarek, J. F., Kader, Z., Kaspi, V., Landecker, T. L., Lanman, A. E., Lazda, M., Leung, C., Lin, H.-H., Masui, K. W., McKinven, R., Mena-Parra, J., Meyers, B. W., Michilli, D., Ng, C., Pandhi, A., Pearlman, A. B., Pen, U.-L., Petroff, E., Pleunis, Z., Rafiei-Ravandi, M., Rahman, M., Ransom, S. M., Renard, A., Sand, K. R., Sanghavi, P., Scholz, P., Shah, V., Shin, K., Siegel, S., Smith, K., Stairs, I., Su, J., Tendulkar, S. P., Vanderlinde, K., Wang, H., Wulf, D., & Zwaniga, A., 2023. CHIME/FRB Discovery of 25 Repeating Fast Radio Burst Sources, *ApJ*, **947**(2), 83.
- CHIME/FRB Collaboration, Abbott, T., Andersen, B. C., Andrew, S., Bandura, K., Bhardwaj, M., Bhusare, Y., Brar, C., Cassanelli, T., Chatterjee, S., Cliche, J.-F., Cook, A. M., Curtin, A., Dobbs, M., Dong, F. A., Eadie, G., Eftekhari, T., Fonseca, E., Gaensler, B. M., Good, D., Halpern, M., Hessels, J. W. T., Ibik, A., Jain, N., Joseph, R. C., Kader, Z., Kaspi, V. M., Khan, A., Kharel, B., Kumar, A., Landecker, T. L., Lang, D., Lanman, A. E., L'Argent, M., Lazda, M., Leung, C., Li, D. Z., Lintott, C. J., Main, R., Masui, K. W., Mate, S., McGregor, K., McKinven, R., Mena-Parra, J., Meyers, B. W., Michilli, D., Ng, C., Ng, M., Nimmo, K., Noble, G., Pandhi, A., Patil, S. S., Pearlman, A. B., Pen, U.-L., Pleunis, Z., Prochaska, J. X., Rafiei-Ravandi, M., Ransom, S., Renard, A., Sammons, M. W., Sand, K. R., Scholz, P., Shah, V., Shin, K., Siegel, S. R., Sirota, S., Smith, K., Stairs, I., Stenning, D. C., Tendulkar, S. P., Vanderlinde, K., Walmsley, M., Wang, H., & Wulf, D., 2026. The Second CHIME/FRB Catalog of Fast Radio Bursts, *arXiv e-prints*, p. arXiv:2601.09399.
- Cordes, J. M. & Chatterjee, S., 2019. Fast Radio Bursts: An Extragalactic Enigma, *ARA&A*, **57**, 417–465.
- DeBoer, D. R., Parsons, A. R., Aguirre, J. E., Alexander, P., Ali, Z. S., Beardsley, A. P., Bernardi, G., Bowman, J. D., Bradley, R. F., Carilli, C. L., Cheng, C., de Lera Acedo, E., Dillon, J. S., Ewall-Wice, A., Fadana, G., Fagnoni, N., Fritz, R., Furlanetto, S. R., Glendenning, B., Greig, B., Grobbelaar, J., Hazeltun, B. J., Hewitt, J. N., Hickish, J., Jacobs, D. C., Julius, A., Kariseb, M., Kohn, S. A., Lekalake, T., Liu, A., Loots, A., MacMahon, D., Malan, L., Malgas, C., Maree, M., Martinot, Z., Mathison, N., Matsetela, E., Mesinger, A., Morales, M. F., Neben, A. R., Patra, N., Pieterse, S., Pober, J. C., Razavi-Ghods, N., Ringuette, J., Robnett, J., Rosie, K., Sell, R., Smith, C., Syce, A., Tegmark, M., Thyagarajan, N., Williams, P. K. G., & Zheng, H., 2017. Hydrogen Epoch of Reionization Array (HERA), *PASP*, **129**(974), 045001.
- Dong, F. A. & Chime/Frb Collaboration, 2022. CHIME/FRB Detection of a Bright Radio Burst from SGR 1935+2154, *The Astronomer's Telegram*, **15681**, 1.
- Ewall-Wice, A., Kern, N., Dillon, J. S., Liu, A., Parsons, A., Singh, S., Lanman, A., La Plante, P., Fagnoni, N., Acedo, E. d. L., DeBoer, D. R., Nunhokee, C., Bull, P., Chang, T.-C., Lazio, T. J. W., Aguirre, J., & Weinberg, S., 2021. DAYENU: a simple filter of smooth foregrounds for intensity mapping power spectra, *MNRAS*, **500**(4), 5195–5213.
- Foreman-Mackey, D., Hogg, D. W., Lang, D., & Goodman, J., 2013. emcee: The MCMC Hammer, *PASP*, **125**(925), 306.
- Giri, U., Andersen, B. C., Chawla, P., Curtin, A. P., Fonseca, E., Kaspi, V. M., Lin, H.-H., Masui, K. W., Sand, K. R., Scholz, P., Abbott, T. C., Dong, F. A., Gaensler, B. M., Leung, C., Michilli, D., Bhardwaj, M., Münchmeyer, M., Pandhi, A., Pearlman, A. B., Pleunis, Z., Rafiei-Ravandi, M., Reda, A., Shin, K., Smith, K., Stairs, I. H., Stenning, D. C., & Tendulkar, S. P., 2023. Comprehensive Bayesian analysis of FRB-like bursts from SGR 1935+2154 observed by CHIME/FRB, *arXiv e-prints*, p. arXiv:2310.16932.
- Hickish, J., Abdurashidova, Z., Ali, Z., Buch, K. D., Chaudhari, S. C., Chen, H., Dexter, M., Domagalski, R. S., Ford, J., Foster, G., George, D., Greenberg, J., Greenhill, L., Isaacson, A., Jiang, H., Jones, G., Kapp, F., Kriel, H., Lacasse, R., Lutomirski, A., MacMahon, D., Manley, J., Martens, A., McCullough, R., Muley, M. V., New, W., Parsons, A., Price, D. C., Primiani, R. A., Ray, J., Siemion, A., van Tonder, V., Vertatschitsch, L., Wagner, M., Weintroub, J., & Werthimer, D., 2016. A Decade of Developing Radio-Astronomy Instrumentation using CASPER Open-Source Technology, *Journal of Astronomical Instrumentation*, **5**(4), 1641001–12.
- Hu, C.-P., Begičarslan, B., Güver, T., Enoto, T., Younes, G., Sakamoto, T., Ray, P. S., Strohmayr, T. E., Guillot, S., Arzoumanian, Z., Palmer, D. M., Gendreau, K. C., Malacaria, C., Wadiasingh, Z., Jaisawal, G. K., & Majid, W. A., 2020. NICER Observation of the Temporal and Spectral Evolution of Swift J1818.0-1607: A Missing Link between Magnetars and Rotation-powered Pulsars, *ApJ*, **902**(1), 1.
- Huang, Y. X., Xu, H., Xu, Y. H., Wang, B. J., Li, Z. X., Zhang, C. F., Xu, J. W., Jiang, J. C., Men, Y. P., Gao, G. N., Xu, Z. H., Hao, L. F., Lee, K. J., Wang, M., Zhang, B., & Zhu, W. W., 2022. An intermediately bright radio burst detected from SGR 1935+2154 in S-band by Yunnan 40m radio telescope, *The Astronomer's Telegram*, **15707**, 1.
- Karuppusamy, R., Stappers, B. W., & van Straten, W., 2010. Giant pulses from the Crab pulsar. A wide-band study, *A&A*, **515**, A36.
- Kirsten, F., Snelders, M. P., Jenkins, M., Nimmo, K., van den Eijnden, J., Hessels, J. W. T., Gawroński, M. P., & Yang, J., 2021. Detection of two bright radio bursts from magnetar SGR 1935 + 2154, *Nature Astronomy*, **5**, 414–422.
- Kirsten, F., Ould-Boukattine, O. S., Herrmann, W., Gawroński, M. P., Hessels, J. W. T., Lu, W., Snelders, M. P., Chawla, P., Yang, J., Blaauw, R., Nimmo, K., Puchalska, W., Wolak, P., & van Ruiten, R., 2024. A link between repeating and non-repeating fast radio bursts through their energy distributions, *Nature Astronomy*, **8**, 337–346.
- Kocz, J., Ravi, V., Catha, M., D'Addario, L., Hallinan, G., Hobbs, R., Kulkarni, S., Shi, J., Vedantham, H., Weinreb, S., & Woody, D., 2019. DSA-10: a prototype array for localizing fast radio bursts, *MNRAS*, **489**(1), 919–927.
- Kumar, P., Lu, W., & Bhattacharya, M., 2017. Fast radio burst source properties and curvature radiation model, *MNRAS*, **468**(3), 2726–2739.
- Lazarus, P., Kaspi, V. M., Champion, D. J., Hessels, J. W. T., & Dib, R., 2012. Constraining Radio Emission from Magnetars, *ApJ*, **744**(2), 97.
- Lewandowska, N., Demorest, P. B., McLaughlin, M. A., Kilian, P., & Hankins, T. H., 2022. Single Pulse Dispersion Measure of the Crab Pulsar, *ApJ*, **935**(2), 84.
- Li, C. K., Lin, L., Xiong, S. L., Ge, M. Y., Li, X. B., Li, T. P., Lu, F. J., Zhang,

- S. N., Tuo, Y. L., Nang, Y., Zhang, B., Xiao, S., Chen, Y., Song, L. M., Xu, Y. P., Liu, C. Z., Jia, S. M., Cao, X. L., Qu, J. L., Zhang, S., Gu, Y. D., Liao, J. Y., Zhao, X. F., Tan, Y., Nie, J. Y., Zhao, H. S., Zheng, S. J., Zheng, Y. G., Luo, Q., Cai, C., Li, B., Xue, W. C., Bu, Q. C., Chang, Z., Chen, G., Chen, L., Chen, T. X., Chen, Y. B., Chen, Y. P., Cui, W., Cui, W. W., Deng, J. K., Dong, Y. W., Du, Y. Y., Fu, M. X., Gao, G. H., Gao, H., Gao, M., Gu, Y. D., Guan, J., Guo, C. C., Han, D. W., Huang, Y., Huo, J., Jiang, L. H., Jiang, W. C., Jin, J., Jin, Y. J., Kong, L. D., Li, G., Li, M. S., Li, W., Li, X., Li, X. F., Li, Y. G., Li, Z. W., Liang, X. H., Liu, B. S., Liu, G. Q., Liu, H. W., Liu, X. J., Liu, Y. N., Lu, B., Lu, X. F., Luo, T., Ma, X., Meng, B., Ou, G., Sai, N., Shang, R. C., Song, X. Y., Sun, L., Tao, L., Wang, C., Wang, G. F., Wang, J., Wang, W. S., Wang, Y. S., Wen, X. Y., Wu, B. B., Wu, B. Y., Wu, M., Xiao, G. C., Xu, H., Yang, J. W., Yang, S., Yang, Y. J., Yang, Y.-J., Yi, Q. B., Yin, Q. Q., You, Y., Zhang, A. M., Zhang, C. M., Zhang, F., Zhang, H. M., Zhang, J., Zhang, T., Zhang, W., Zhang, W. C., Zhang, W. Z., Zhang, Y., Zhang, Y., Zhang, Y. F., Zhang, Y. J., Zhang, Z., Zhang, Z., Zhang, Z. L., Zhou, D. K., Zhou, J. F., Zhu, Y., Zhu, Y. X., & Zhuang, R. L., 2021. HXMT identification of a non-thermal X-ray burst from SGR J1935+2154 and with FRB 200428, *Nature Astronomy*, **5**, 378–384.
- Li, D., Wang, P., Qian, L., Krco, M., Jiang, P., Yue, Y., Jin, C., Zhu, Y., Pan, Z., Nan, R., & Dunning, A., 2018. FAST in Space: Considerations for a Multibeam, Multipurpose Survey Using China's 500-m Aperture Spherical Radio Telescope (FAST), *IEEE Microwave Magazine*, **19**(3), 112–119.
- Lorimer, D. R., Bailes, M., McLaughlin, M. A., Narkevic, D. J., & Crawford, F., 2007. A Bright Millisecond Radio Burst of Extragalactic Origin, *Science*, **318**(5851), 777.
- Lu, W., Kumar, P., & Zhang, B., 2020. A unified picture of Galactic and cosmological fast radio bursts, *MNRAS*, **498**(1), 1397–1405.
- Lyne, A. G., Pritchard, R. S., & Graham Smith, F., 1993. 23 years of Crab pulsar rotational history., *MNRAS*, **265**, 1003–1012.
- Maan, Y. & van Leeuwen, J., 2017. Real-time searches for fast transients with Apertif and LOFAR, in *2017 XXXIInd General Assembly and Scientific Symposium of the International Union of Radio Science (URSI GASS)*, p. 2.
- Maan, Y., Leeuwen, J. v., Straal, S., & Pastor-Marazuela, I., 2022. GBT detection of bright 5 GHz radio bursts from SGR 1935+2154, coincident with X-ray and 600 MHz bursts, *The Astronomer's Telegram*, **15697**, 1.
- Majid, W. A., Naudet, C. J., Lowe, S. T., & Kuiper, T. B. H., 2011. Statistical Studies of Giant Pulse Emission from the Crab Pulsar, *ApJ*, **741**(1), 53.
- Margalit, B., Beniamini, P., Sridhar, N., & Metzger, B. D., 2020. Implications of a Fast Radio Burst from a Galactic Magnetar, *ApJ*, **899**(2), L27.
- McKee, J. W., Lyne, A. G., Stappers, B. W., Bassa, C. G., & Jordan, C. A., 2018. Temporal variations in scattering and dispersion measure in the Crab Pulsar and their effect on timing precision, *MNRAS*, **479**(3), 4216–4224.
- Mereghetti, S., Savchenko, V., Ferrigno, C., Götz, D., Rigoselli, M., Tiengo, A., Bazzano, A., Bozzo, E., Coleiro, A., Courvoisier, T. J.-L., Doyle, M., Goldwurm, A., Hanlon, L., Jourdain, E., von Kienlin, A., Lutovinov, A., Martin-Carrillo, A., Molokov, S., Natalucci, L., Onori, F., Panessa, F., Rodi, J., Rodriguez, J., Sánchez-Fernández, C., Sunyaev, R., & Ubertini, P., 2020. INTEGRAL Discovery of a Burst with Associated Radio Emission from the Magnetar SGR 1935+2154, *ApJ*, **898**(2), L29.
- Metzger, B. D., Margalit, B., & Sironi, L., 2019. Fast radio bursts as synchrotron maser emission from decelerating relativistic blast waves, *MNRAS*, **485**(3), 4091–4106.
- Niu, C.-H., Li, D., Luo, R., Wang, W.-Y., Yao, J., Zhang, B., Zhu, W.-W., Wang, P., Ye, H., Zhang, Y.-K., Niu, J.-r., Tang, N.-y., Duan, R., Krco, M., Dai, S., Feng, Y., Miao, C., Pan, Z., Qian, L., Xue, M., Yuan, M., Yue, Y., Zhang, L., & Zhang, X., 2021. CRAFTS for Fast Radio Bursts: Extending the Dispersion-Fluence Relation with New FRBs Detected by FAST, *ApJ*, **909**(1), L8.
- Olausen, S. A. & Kaspi, V. M., 2014. The McGill Magnetar Catalog, *ApJS*, **212**(1), 6.
- Ostrom, L. C., Maan, Y., van Leeuwen, J., Connor, L., Petroff, E., Attema, J. J., Bast, J. E., Gardener, D. W., Hargreaves, J. E., Kooistra, E., van der Schuur, D., Sclocco, A., Smits, R., Straal, S. M., ter Veen, S., Vohl, D., Adams, E. A. K., Adebahr, B., de Blok, W. J. G., van den Brink, R. H., van Cappellen, W. A., Coolen, A. H. W. M., Damstra, S., van Diepen, G. N. J., Frank, B. S., Hess, K. M., van der Hulst, J. M., Hut, B., Ivashina, M. V., Loose, G. M., Lucero, D. M., Mika, Á., Morganti, R. H., Moss, V. A., Mulder, H., Norden, M. J., Oosterloo, T. A., Orrù, E., de Reijer, J. P. R., Ruitter, M., Vermaas, N. J., Wijnholds, S. J., & Ziemke, J., 2020. Repeating fast radio bursts with WSRT/Apertif, *A&A*, **635**, A61.
- Parsons, A., 2009. The Symmetric Group in Data Permutation, With Applications to High-Bandwidth Pipelined FFT Architectures, *IEEE Signal Processing Letters*, **16**(6), 477–480.
- Pearlman, A. B. & Chime/Frb Collaboration, 2022. CHIME/FRB Detection of Another Bright Radio Burst from SGR 1935+2154, *The Astronomer's Telegram*, **15792**, 1.
- Petroff, E., Barr, E. D., Jameson, A., Keane, E. F., Bailes, M., Kramer, M., Morello, V., Tabbara, D., & van Straten, W., 2016. FRBCAT: The Fast Radio Burst Catalogue, *Publ. Astron. Soc. Australia*, **33**, e045.
- Price, D. C., 2016. PyGDSM: Python interface to Global Diffuse Sky Models, Astrophysics Source Code Library, record ascl:1603.013.
- Ridnaia, A., Svinin, D., Frederiks, D., Bykov, A., Popov, S., Aptekar, R., Golenetskii, S., Lysenko, A., Tsvetkova, A., Ulanov, M., & Cline, T. L., 2021. A peculiar hard X-ray counterpart of a Galactic fast radio burst, *Nature Astronomy*, **5**, 372–377.
- Shannon, R. M., Macquart, J.-P., Bannister, K. W., Ekers, R. D., James, C. W., Osłowski, S., Qiu, H., Sammons, M., Hotan, A. W., Voronkov, M. A., Beresford, R. J., Brothers, M., Brown, A. J., Bunton, J. D., Chippendale, A. P., Haskins, C., Leach, M., Marquarding, M., McConnell, D., Pilawa, M. A., Sadler, E. M., Troup, E. R., Tuthill, J., Whiting, M. T., Allison, J. R., Anderson, C. S., Bell, M. E., Collier, J. D., Gürkan, G., Heald, G., & Riseley, C. J., 2018. The dispersion-brightness relation for fast radio bursts from a wide-field survey, *Nature*, **562**(7727), 386–390.
- Sheikh, S. Z., Farah, W., Pollak, A. W., Siemion, A. P. V., Chamma, M. A., Cruz, L. F., Davis, R. H., DeBoer, D. R., Gajjar, V., Karn, P., Kittling, J., Lu, W., Masters, M., Premnath, P., Schoultz, S., Shumaker, C., Singh, G., & Snodgrass, M., 2024. Characterization of the repeating FRB 20220912A with the Allen Telescope Array, *MNRAS*, **527**(4), 10425–10439.
- Shi, J., Weinreb, S., Zhong, W., Yin, X., & Yang, M., 2017. Quadruple-Ridged Flared Horn Operating From 8 to 50 GHz, *IEEE Transactions on Antennas and Propagation*, **65**(12), 7322–7327.
- Shin, K., Masui, K. W., Bhardwaj, M., Cassanelli, T., Chawla, P., Dobbs, M., Dong, F. A., Fonseca, E., Gaensler, B. M., Herrera-Martín, A., Kaczmarek, J., Kaspi, V., Leung, C., Merryfield, M., Michilli, D., Münchmeyer, M., Pearlman, A. B., Rafei-Ravandi, M., Smith, K., Stairs, I., & Tendulkar, S. P., 2023. Inferring the Energy and Distance Distributions of Fast Radio Bursts Using the First CHIME/FRB Catalog, *ApJ*, **944**(1), 105.
- Shitov, Y. P., 1999. SGR 1900+14 = PSR J1907+0919, *IAU Circ.*, **7110**, 2.
- Spitler, L. G., Scholz, P., Hessels, J. W. T., Bogdanov, S., Brazier, A., Camilo, F., Chatterjee, S., Cordes, J. M., Crawford, F., Deneva, J., Ferdman, R. D., Freire, P. C. C., Kaspi, V. M., Lazarus, P., Lynch, R., Madsen, E. C., McLaughlin, M. A., Patel, C., Ransom, S. M., Seymour, A., Stairs, I. H., Stappers, B. W., van Leeuwen, J., & Zhu, W. W., 2016. A repeating fast radio burst, *Nature*, **531**(7593), 202–205.
- Thornton, D., Stappers, B., Bailes, M., Barsdell, B., Bates, S., Bhat, N. D. R., Burgay, M., Burke-Spolaor, S., Champion, D. J., Coster, P., D'Amico, N., Jameson, A., Johnston, S., Keith, M., Kramer, M., Levin, L., Milia, S., Ng, C., Possenti, A., & van Straten, W., 2013. A Population of Fast Radio Bursts at Cosmological Distances, *Science*, **341**(6141), 53–56.
- Welch, J., Backer, D., Blitz, L., Bock, D. C.-J., Bower, G. C., Cheng, C., Croft, S., Dexter, M., Engargiola, G., Fields, E., Forster, J., Gutierrez-Kraybill, C., Heiles, C., Helfer, T., Jorgensen, S., Keating, G., Lugten, J., MacMahon, D., Milgrome, O., Thornton, D., Urry, L., van Leeuwen, J., Werthimer, D., Williams, P. H., Wright, M., Tarter, J., Ackermann, R., Atkinson, S., Backus, P., Barott, W., Bradford, T., Davis, M., Deboer, D., Dreher, J., Harp, G., Jordan, J., Kilsdonk, T., Pierson, T., Randall, K., Ross, J., Shostak, S., Fleming, M., Cork, C., Vitouchkine, A., Wadefalk, N., & Weinreb, S., 2009. The Allen Telescope Array: The First Widefield, Panchromatic, Snapshot Radio Camera for Radio Astronomy and SETI,

*IEEE Proceedings*, **97**(8), 1438–1447.

- Younes, G., Lander, S. K., Baring, M. G., Bause, M. L., Stewart, R., Arzoumanian, Z., Thi, H. D., Enoto, T., Gendreau, K. C., Güver, T., Harding, A. K., Ho, W. C. G., Hu, C.-P., Van Kooten, A., Kouveliotou, C., Di Lalla, N., McEwen, A., Negro, M., Ng, M., Palmer, D. M., Spitler, L. G., & Wadiasingh, Z., 2025. Timing and Spectral Evolution of the Magnetar 1E 1841-045 in Outburst, *ApJ*, **989**(1), 89.
- Zackay, B. & Ofek, E. O., 2017. An Accurate and Efficient Algorithm for Detection of Radio Bursts with an Unknown Dispersion Measure, for Single-dish Telescopes and Interferometers, *ApJ*, **835**(1), 11.
- Zhang, C. F., Jiang, J. C., Men, Y. P., Wang, B. J., Xu, H., Xu, J. W., Niu, C. H., Zhou, D. J., Guan, X., Han, J. L., Jiang, P., Lee, K. J., Li, D., Lin, L., Niu, J. R., Wang, P., Wang, Z. L., Xu, R. X., Yu, W., Zhang, B., & Zhu, W. W., 2020. A highly polarised radio burst detected from SGR 1935+2154 by FAST, *The Astronomer's Telegram*, **13699**, 1.
- Zhu, W., Xu, H., Zhou, D., Lin, L., Wang, B., Wang, P., Zhang, C., Niu, J., Chen, Y., Li, C., Meng, L., Lee, K., Zhang, B., Feng, Y., Ge, M., Göğüş, E., Guan, X., Han, J., Jiang, J., Jiang, P., Kouveliotou, C., Li, D., Miao, C., Miao, X., Men, Y., Niu, C., Wang, W., Wang, Z., Xu, J., Xu, R., Xue, M., Yang, Y., Yu, W., Yuan, M., Yue, Y., Zhang, S., & Zhang, Y., 2023. A radio pulsar phase from SGR J1935+2154 provides clues to the magnetar FRB mechanism, *Science Advances*, **9**(30), eadf6198.

## APPENDIX A: CANDIDATE LIMBO FRBS

Of the 24 events with detection significances  $\geq 5.6$  obtained during the May-August 2023 LIMBO observing campaign of SGR 1935+2154, 12 events are classified as candidate FRB detections. Their power spectra are shown in Figure A1, where each pulse is dedispersed to maximize its SNR. Pulse properties, such as dispersion measure, fluence, SNR, and Z-score are provided in Table 3.

## APPENDIX B: RFI-INDUCED FALSE-POSITIVE TRIGGERS

Of the remaining 12 events with  $Z \geq 5.6$ , 7 are identified to be consistent with false-positive triggers due to spurious RFI contamination. Three representative spectra are shown in the top row of Figure B1. Broad or variable time and frequency structure exhibited in these spectra is inconsistent with that expected for FRBs, motivating their removal from the detection sample. Diagonal, high-contrast features in the dynamic spectra are artifacts of the LIMBO RFI-rejection pipeline, which flags RFI-contaminated regions, inpaints them with Gaussian noise, and subsequently dedisperses the data.

The remaining 3 candidates exhibit mixed morphology, combining FRB-like features with clear signatures of RFI (Figure B1 (*bottom*)). Because these events are more ambiguous and LIMBO does not currently implement a recovery pipeline for these types of events, they are also removed from the final detection sample.

This paper has been typeset from a  $\text{\TeX}/\text{\LaTeX}$  file prepared by the author.

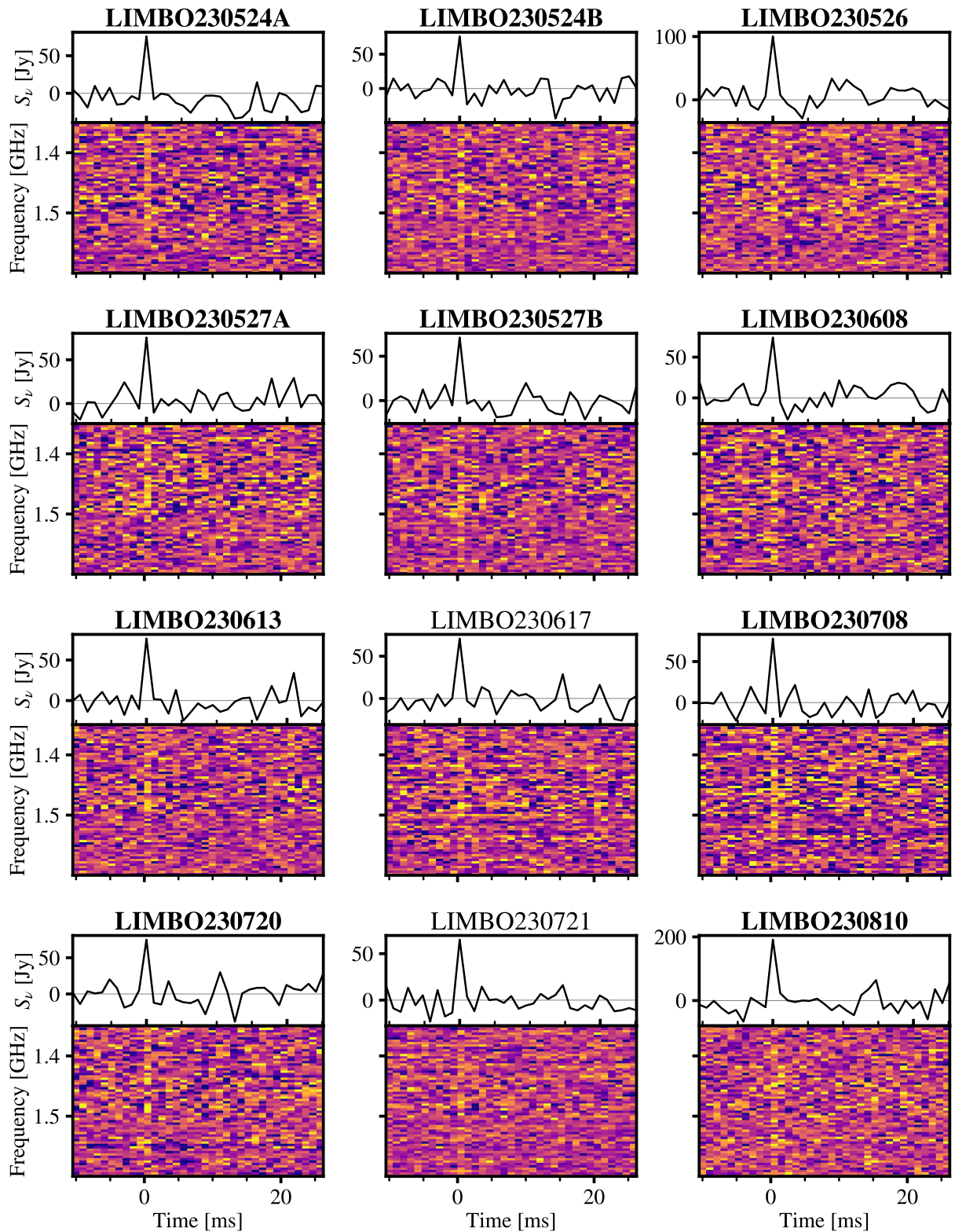


**Figure A1.** The power spectra of bursts detected by LIMBO from Galactic magnetar SGR 1935+2154, tentatively classified as candidate FRBs. In each figure, the top panel shows the frequency-averaged flux density as a function of time, while the bottom panel displays the burst in both frequency and time domain. Bursts with bolded names represent the events we are most confident in classifying as candidate FRB detections. Each pulse is dedispersed to maximize its SNR. Pulse properties are given in Table 3.

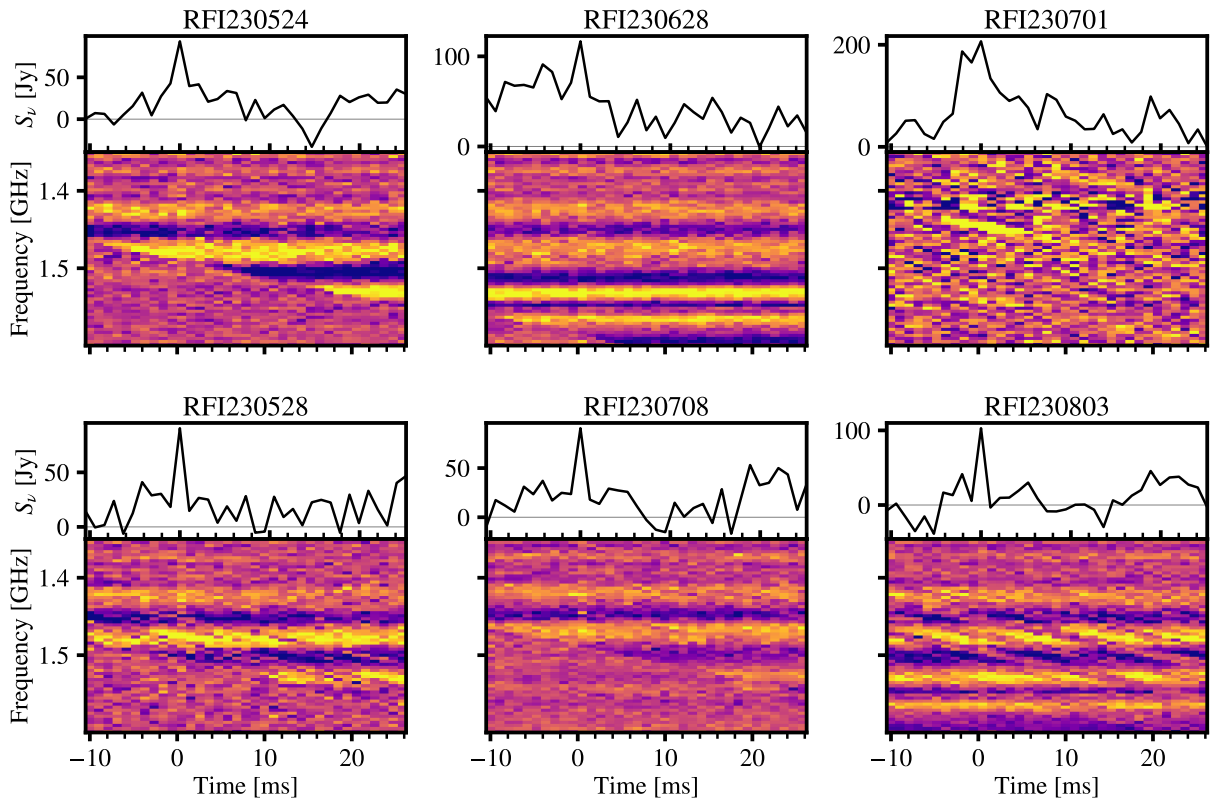


**Figure B1.** *Top:* Example spectra from typical RFI-induced false-positive triggers from the LIMBO system. The diagonal contrast seen in the dynamic spectrum of RFI230524 and RF230628 is an artifact of the LIMBO RFI excision pipeline’s flagging and inpainting procedures. The variability in both time and frequency are quite different from the behaviour expected of FRBs, making it easy to visually distinguish these events as false-positive triggers. *Bottom:* RFI-classified events with possible underlying FRB candidates. Inpainting and RFI contamination make analysing these events difficult. These events are therefore excluded from the larger FRB candidate sample as LIMBO does not yet have means to recover FRB-like bursts from files heavily contaminated with overlying RFI.